Arch Toxicol (2017) 91:3011–3037
DOI 10.1007/s00204-017-2016-8

REVIEW ARTICLE

Toxic effects and biodistribution of ultrasmall gold nanoparticles

Günter Schmid[1] · **Wolfgang G. Kreyling**[2] · **Ulrich Simon**[3]

Received: 16 May 2017 / Accepted: 13 June 2017 / Published online: 12 July 2017
© Springer-Verlag GmbH Germany 2017

Abstract Gold nanoparticles (AuNPs) have been extensively explored in biomedical applications, for example as drug carriers, contrast agents, or therapeutics. However, AuNP can exhibit cytotoxic profile, when the size is below 2 nm (ultrasmall AuNP; usAuNP) and when the stabilizing ligands allow for access to the gold surface either for the direct interaction with biomolecules or for catalytic activity of the unshielded gold surface. Furthermore, usAuNP exhibits significantly different biodistribution and enhanced circulation times compared to larger AuNP. This review gives an overview about the synthesis and the physicochemical properties of usAuNP and, thereby, focusses on 1.4 nm sized AuNP, which are derived from the compound $Au_{55}(PPh_3)_{12}Cl_6$ and which are the most intensively studied usAuNP in the field. This part is followed by a summary of the toxic properties of usAuNP, which include in vitro cytotoxicity tests on different cell lines, electrophysiological tests following FDA guidelines as well as studies on antibacterial effects. Finally, the biodistribution and pharmacokinetics of ultrasmall AuNP are discussed and compared to the properties of more biocompatible, larger AuNP.

Keywords Gold nanoparticle · Cytotoxicity · Biodistribution · Pharamcokinetics

✉ Günter Schmid
Guenter.Schmid@uni-due.de

[1] Institute of Inorganic Chemistry, University Duisburg-Essen, Universitätsstr. 5-7, 45127 Essen, Germany

[2] Helmholtz Zentrum München, German Research Center for Environmental Health, Institute of Epidemiology 2, Ingolstaedter Landstrasse 1, Neuherberg, 85764 Munich, Germany

[3] Institute of Inorganic Chemistry, RWTH Aachen University, Landoltweg 1a, 52074 Aachen, Germany

Introduction

Gold in its macroscopic (bulk) state is known to be highly unreactive and is thus considered the noblest of all the metals (Hammer and Norskov 1995). It is, therefore, the material of choice in various medical procedures, including reconstructive surgery, drug delivery microchips, endovascular stents, or as dental prostheses (Demann et al. 2005) and is applied as a food additive labeled by the E number 175 (EFSA 2016). In its ionic state, as constituent of gold salts or molecular complexes, gold is a reactive metal, which, in turn, can also be utilized for therapeutic purposes, e.g., for the treatment of rheumatoid arthritis, where gold(I) thiolates are the principal compounds (Shaw 1999). Between the bulk and the molecular state, a new avenue is opened by nanometer sized gold particles (gold nanoparticles; AuNPs), which exhibit physico-chemical properties, which may differ drastically from the bulk and molecular state and that are characterized by properties, that are determined by size as an independent parameter (Broda et al. 2014; Daniel and Astruc 2004; Schmid and Simon 2005). AuNPs are likewise easy to synthesize, they are tunable in size (they typically span a size range from 1–100 nm in diameter) and shape, including spheres, rods, hollows spheres, cubes etc. (Grzelczak et al. 2008). Besides the most striking feature, namely the increasing rate of surface atoms compared to bulk atoms with decreasing size as a general feature of nanoparticles, other properties are determined by the particles size, such as the melting point (Schmid and Corain 2003) or the electronic structure (Häkkinen 2008), which are invariant with size in the bulk state.

An optical property that appears on the nanoscale is the so-called surface plasmon resonance (SPR) (El-Sayed 2003), which will be explained briefly below. The spectral position of the SPR can be adjusted via size and shape of

the AuNP, which has led to several new biomedical applications in diagnostics, such as bimolecular sensing (Schmid and Corain 2003). Meanwhile, therapeutic applications are being discussed in the literature as well, which utilize the SPR, e.g., for photoacoustic imaging (Li and Chen 2015) or NIR-responsive controlled release (Yavuz et al. 2009).

The perspective to explore applications in vivo as well as the fact, that AuNP are increasingly applied in technical environments, for examples as catalysts (Tyo and Vajda 2015) or as building blocks in nanoelectronic devices (Homberger and Simon 2010), concerns arise with respect to potential toxicities, as this may lead to unintended (and thereby uncontrolled) instead of intended (controlled) exposure. This has prompted numerous studies on the size-dependent cytotoxicity of AuNP in vitro and in vivo (e.g., Alkilany and Murphy 2010; Jia et al. 2017; Lewinski et al. 2008; Soenen et al. 2012) that covered the above-mentioned size range below 100 nm and that included different surface ligands, that need to be applied to stabilize the particles in solution and to prevent them from agglomeration in biological media. Most of the toxicity studies considered AuNPs, which are stabilized by organic molecules carrying thiol moieties, which allow for strong anchoring of the ligand to the AuNP's surface. Furthermore, the increasing use of AuNP in medical and technical fields leads to increasing exposure in many occupations but also of consumers and, therefore, the public at large and patients being exposed with novel AuNP containing medication for diagnostics and therapy (Stone et al. 2016). Exposures of consumers are dominated mainly via ingestion but also via inhalation, whereas exposure of patients occurs via injections mostly intravenously and also via ingestions, depending on the prescribed medications. Dermal exposures may occur; however, the existing evidence suggests that intake through the skin is usually not detectable.

As a result of possible exposures, the organs of intake are the respiratory tract, the digestive tract and blood circulation. In recent years, it became evident that not only the organs of intake will be exposed but also secondary organs like liver, spleen, kidneys, heart, brain, the reproductive system, and also tissues like those of the skeleton, the central nervous system and the immune-competent system. Twenty years ago, particularly, the exposure of secondary organs and tissues was believed to be negligible, since the masses of nanoparticles, including AuNP, were so minute that any mass concentration-based adverse health effects in secondary organs were dismissed. Meanwhile, nanotoxicological research demonstrated that nanoparticles can pose risks according to their unique physico-chemical properties such as their specific surface area, their very large number of individual particles, and their increased reactivity with biological fluids and tissues. In addition, cardio-vascular effects observed in epidemiological studies triggered the discussion on enhanced translocation of ultrafine particles from the respiratory epithelium towards the circulation and subsequent organs, such as heart, liver, spleen and brain, eventually causing adverse effects on cardiac function and blood coagulation, as well as on functions of the central nervous system. There is clear evidence that NP can cross body membranes and reach the above-mentioned secondary organs and accumulate there, as most recently demonstrated by Miller et al., who showed that inhaled AuNP may accumulate at sites of vascular disease (Miller et al. 2017).

However, to this date, the understanding of the bioactivity and biodistribution of AuNP, taking in account the particles size as a dominant parameter together with the composition (charge, polarity, thickness, etc.) of the ligand shell and its binding characteristics between gold surface and ligand molecule, still requires well-designed and interdisciplinary research and, eventually, re-evaluation of the existing data. Thereby, apparent inconsistencies in toxicological evaluation, which arise from different experimental conditions (cell lines, animal models, etc.), exposure times, doses and different experimental methods to determine the distribution and fate of the applied AuNP, need to be clarified. Hence, the present state of knowledge is sometimes characterized by conflicting conclusions, so that toxicity issues either resulting from intended or unintended exposure are still under debate (Khlebtsov and Dykman 2011).

Irrespective of the lack of a systematic toxicological and pharmacokinetic classification of the continuously increasing group and diversity of AuNP synthesized, it became evident that in particular usAuNP in the size range below 2 nm can develop a toxic profile (Leifert et al. 2013b). In this context, the size-dependent cytotoxicity of AuNP stabilized by sodium 3-(diphenylphosphino)benzene sulfonate (TPPMS) ligands was reported, whereby the highest toxicity was observed for usAuNP, having a core diameter of 1.4 nm (Au1.4MS). Smaller and larger TPPMS capped and glutathione (GSH) or thioglucose (e.g., used as ligand in the commercial product Aurovist) capped AuNP of similar size were much less toxic. In addition, in patch clamp experiments, particularly Au1.4MS showed irreversible blocking of potassium ion channels (hERG channels), whereas thiol-stabilized AuNP of similar size did not.

A key to understand these unexpected findings is twofold: (1) the extraordinary stability of the 1.4 nm-sized gold core, which is obtained as a water-soluble derivative of the gold cluster $Au_{55}(PPh_3)_{12}Cl_6$ (Au_{55}). Au_{55} is a so-called full-shell cluster, with a gold core consisting of 55 gold atoms, and exhibiting size-specific physico-chemical properties, including high catalytic activity in oxidation reactions with dioxygen (Turner et al. 2008) and a discrete electronic structure that places the cluster in the intermediate state between a metal and a molecule (Schmid 2008). (2) The specific binding situation between AuNP and ligands.

In general, AuNPs need to be stabilized by ligands which have to be electron donors (Lewis base) binding coordinatively and via van der Waals forces to surface atoms of the NPs (Lewis acid) (Reimers et al. 2017). The ligands may be carboxylic acids, amines, phosphines and thiols, whereas the ligand-to-metal binding strength follows the order O < N < P < S, according to the Pearson's Hard and Soft Acids and Bases (HSAB) concept. The toxicity effect of the 1.4 nm-sized AuNP were abolished when the phosphine ligands were replaced AuNP by thiols having a stronger binding affinity to the gold surface and providing a more stable shielding of the gold core towards the biological environment.

This illustrates that AuNP can exhibit cytotoxic profile, when the size is below 2 nm and when the stabilizing ligands allow for direct access to the gold surface either for the direct interaction with biomolecules or for catalytic activity of the unshielded gold surface. As an additional size-dependent feature, Au1.4MS showed in in vivo experiments significantly different biodistribution, and enhanced circulation times compared to larger AuNP (Semmler-Behnke et al. 2008). While the larger particles accumulated in the liver, 1.4 nm AuNPs were detected in other organs as well, which is considered essential for any kind of therapeutic application of usAuNPs (Hirn et al. 2011).

By focusing on these findings, this article gives an overview about the synthesis, the physico-chemical properties, the cytotoxicity studies as well as of the biodistribution and pharmacokinetics of usAuNP, in particular of Au1.4MS as the key compound.

Synthesis of ultrasmall gold nanoparticles, in particular $Au_{55}(PPh_3)_{12}Cl_6$

Syntheses

The synthesis of $Au_{55}(PPh_3)_{12}Cl_6$, in the following called 1.4 nm AuNP, has been published the first time in 1981 (Schmid 1994, 2004). The transition from bulk gold to nanoparticles (earlier called colloids) is not only the reduction in size, but numerous other things change, for instance the melting point and the color. As Fig. 1 impressively shows, the transition from bulk gold to colloids is accompanied by the change of the well-known golden color to ruby red. This effect, known since ancient years, is often used to color glasses.

The original synthesis of the 1.4 nm AuNP is depicted in Fig. 2. It is performed from $(PPh_3)AuCl$ and B_2H_6 in toluene (Schmid et al. 1981). Other substituents on the surface, necessary for protection and preventing coalescence, are monosulfonated phosphines, making the cluster water soluble, alternatively the SH-functionalized

Fig. 1 The color of metallic gold and gold nanoparticles in ruby glass. Reprinted from ref. Corain et al. (2008) with permission from Elsevier Science

(cyclopentyl)$_7Si_8O_{12}(CH_2)_3SH$ (T_8-OSS-SH), or the doubly charged $[B_{12}H_{11}SH]^{2-}$ can be used to substitute PPh_3 and are shown in Fig. 3 (Schmid 2008).

The reason for the phenomenon of color change is best explained by the Mie theory (Mie 1908). It is based on the appearance of a plasmon resonance. This is strictly related to a distinct size of the corresponding metal. On the other hand, this phenomenon is based on the presence of a confined electron gas interacting with light. A simplified explanation is shown in Fig. 4.

Synthesis of the ruby red AuNPs, which are larger than the 1.4 nm Au_{55} cluster, is available by chemical reduction of metal salts including electrochemical pathways (Fu et al. 2002; Ohde et al. 2002; Henglein 2000; Li et al. 2000; Narayanan and El-Sayed 2004; Crooks et al. 2001) or thermolysis (Tano et al. 1989; Esumi et al. 1989, 1990, 1991, 1992a, b).

On the contrary to the larger, in solution red colored AuNPs, $Au_{55}(PPh_3)_{12}Cl_6$ appears brown to yellowish in solution, dependent on the concentration. This is due to its molecular character. The Mie theory is no longer valid in this case.

The 1.4 nm AuNP belongs to the so-called full-shell clusters of the general formula $10n^2 + 2$, whereas n is the shell number. They consist either of cuboctahedral or icosahedral structure. Figure 5 shows the formation of cuboctahedrally structured full-shell clusters.

The first metal atom can be coordinated by 12 equivalent atoms leading to a one-shell cluster consisting of 13 atoms. 13 atoms as a nucleus plus 42 additional Au atoms result in a two-shell cluster of 55 atoms. These clusters should be monodisperse; of course, it cannot be differentiated if there are 55, 54 or 56 atoms, but the monodispersity can be followed from TEM investigations. Figure 5a shows a TEM image of a single Au_{55} cluster and Fig. 6b shows a monolayer of Au_{55} clusters with magnified cutouts.

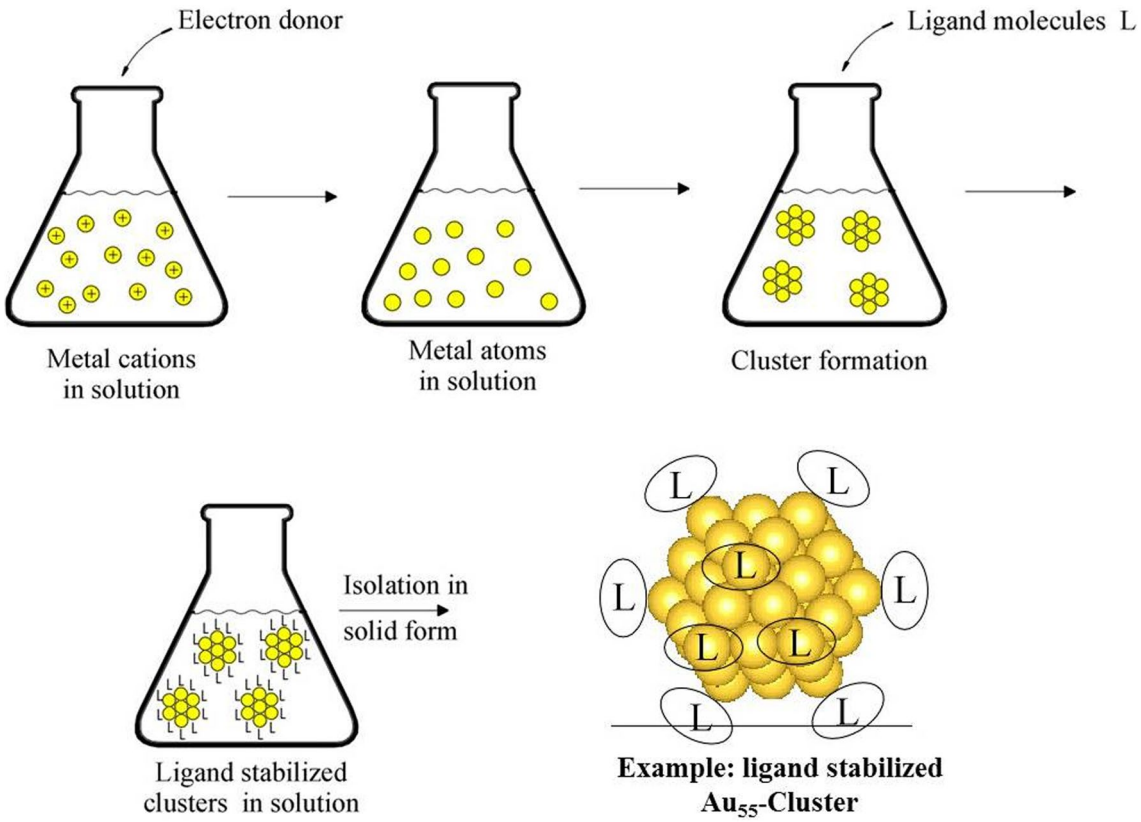

Fig. 2 Synthesis of $Au_{55}(PPh_3)_{12}Cl_6$ from $(PPh_3)AuCl$ and B_2H_6

Electronic properties

Why is the 1.4 nm Au cluster so special? The reason for its special behavior is to be seen in the electronic behavior. It can be described as the transition between bulk and molecule. The stability of the two-shell cluster $Au_{55}(PPh_3)_{12}Cl_6$ results from an impressive experiment. Surface deposited Au_{55} clusters, separated from each other, and compared with smaller and larger Au clusters, are treated with an oxygen plasma to remove the ligand shell. X-ray photoelectron spectroscopy (XPS) shows changes of all other particles, but not of Au_{55} (Boyen et al. 2002). Figure 7 shows the results. Au_{55} only shows a weak oxidic shoulder of a few clusters that are not exactly of full-shell type. All other species show well-expressed signals for oxidic species. This method can, therefore, be used to check the purity of a sample of $Au_{55}(PPh_3)_{12}Cl_6$.

Whereas in a bulk metal, the electrons are distributed in so-called electronic bands. In small molecules like $Fe_3(CO)_{12}$ or $Co_4(CO)_{12}$ the electrons are located in the so-called molecular orbitals. The important question is: Where is the transition from bulk to molecule? Obviously, $Au_{55}(PPh_3)_{12}Cl_6$ performs all necessary conditions at room temperature. At low temperatures, larger particles also fulfill all the conditions to serve as intermediates between bulk and molecule. Figures 8 and 9 show current (*I*)–voltage (*U*) results that clearly show the situation.

Figure 8 shows the *I*–*U* behavior of a 17 nm Pd particle at 295 K and at 4.2 K. At 295, it shows linear metallic behavior, following Ohm's law, whereas at 4.2 K there is a step, called Coulomb blockade (Bezryadin et al. 1997).

Figure 9 proves that $Au_{55}(PPh_3)_{12}Cl_6$ already shows a Coulomb blockade at room temperature (Chi et al. 1998).

The experimental setup to investigate such *I*–*U* characteristics is shown in Fig. 10. It consists of a scanning tunneling microscopy (STM) tip and a conductive surface. In between, there is a single cluster molecule.

An STM image of $Au_{55}(PPh_3)_{12}Cl_6$ is shown in Fig. 11 together with a model of the nanoparticle (Zhang et al. 2003).

Due to the low temperature, the Coulomb blockade is larger than at room temperature (see Fig. 9). In Fig. 12, the *I*–*U* characteristic is changed: the first ablation d*I*/d*U* is used instead of *I* and Coulomb blockade is indicated as a minimum. As can be seen from Fig. 12, this minimum is characterized by a series of energy levels with average spacings of 170 mV. In contrast to the bulk state, the energy bands have disappeared.

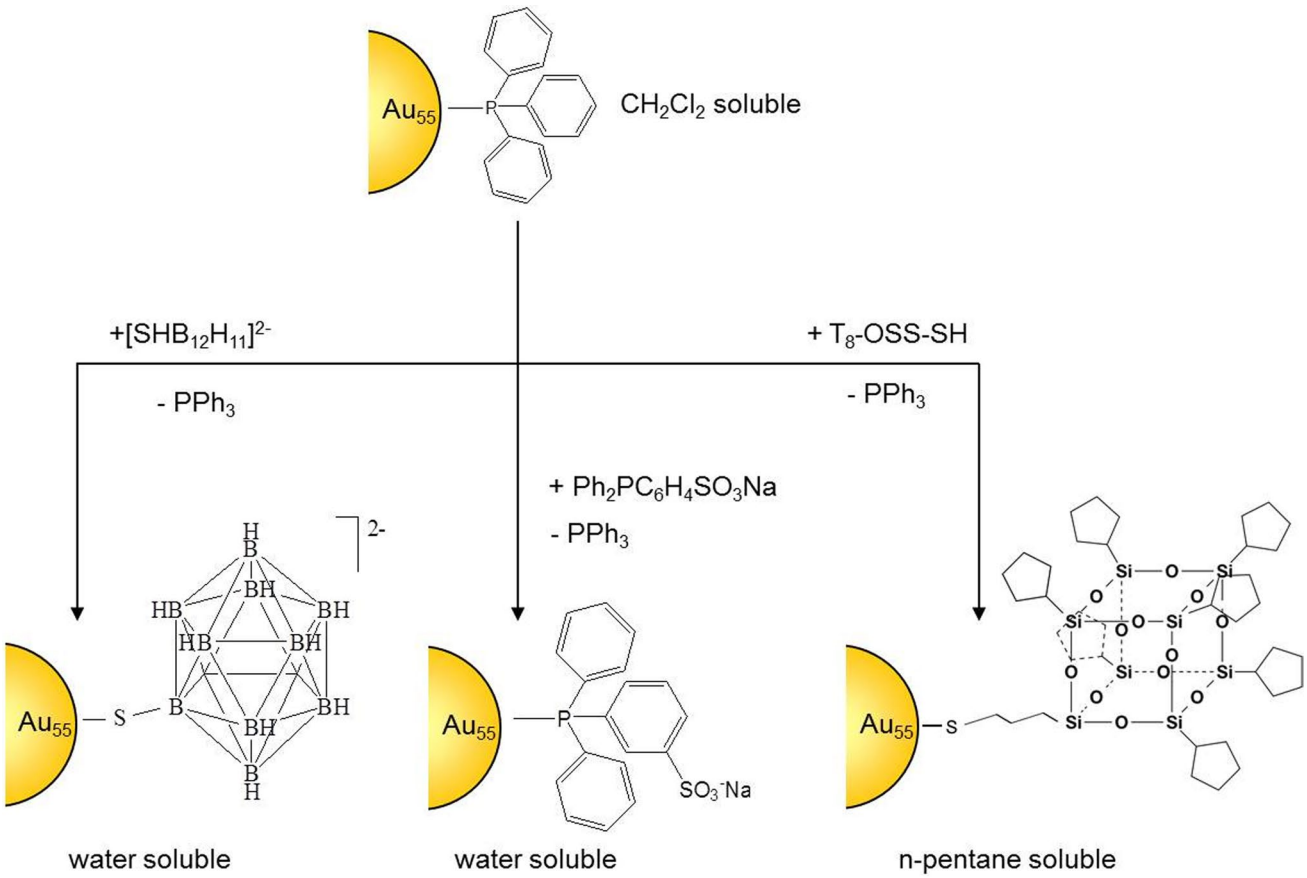

Fig. 3 Substitution of PPh_3 in $Au_{55}(PPh_3)_{12}Cl_6$, generating hydrophilic or hydrophobic character. Reprinted from ref. Schmid (2008) with permission from the Royal Society of Chemistry

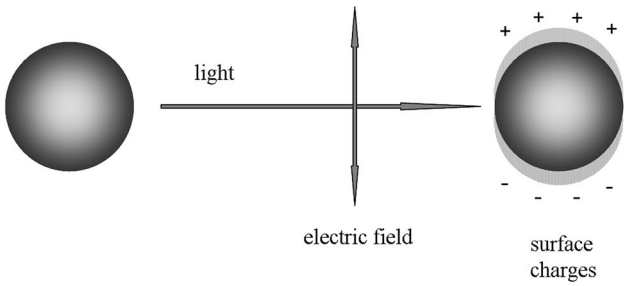

Fig. 4 Illustration of the interaction of visible light and the confined electron gas of a metal nanoparticle, leading to a plasmon resonance, ruby red in case of gold. Reprinted from ref. Corain et al. (2008) with permission from Elsevier

Another method, characterizing the Au_{55} core in $Au_{55}(PPh_3)_{12}Cl_6$, is to study the relaxation behavior of excited electrons and to compare it with other AuNPs (Smith et al. 1997). Femtosecond laser spectroscopy is the corresponding technique. The relaxation time depends on the electron–phonon coupling and on the electron surface collision of electrons. The experimental results concerning the femtosecond laser spectroscopy of AuNPs of different sizes are shown in Fig. 13 (Smith et al. 1997). Weakening of the electron–phonon coupling dominates in large particles slowing down electronic relaxation (see Fig. 13, 15 nm particle). The 1.4 nm Au_{55} nucleus is characterized by strong surface collisions, making relaxation faster. In the case of the 0.7 nm AuNP (Au_{13}), the extremely slow relaxation behavior arises from the fact that the electrons are strictly located in the Au–Au bonds.

These results prove impressively that Au_{55} is just one step before the molecular state and differs characteristically from the 15 nm AuNPs and especially from the bulk.

The last experimental study to prove the extraordinary position of the 1.4 nm $Au_{55}(PPh_3)_{12}Cl_6$ cluster consists of EXAFS studies at 80 K. The results show that the bond lengths in the cluster are significantly shorter than that in bulk gold, indicating a cuboctrahedral packing of the Au atoms. Comparable results were obtained for the water-soluble cluster $Au_{55}(Ph_2PC_6H_4SO_3Na)_{12}Cl_6$, i.e., Au1.4MS (Cluskey et al. 1993).

The conclusion of these experimental results finally is that $Au_{55}(PPh_3)_{12}Cl_6$ and its derivatives occupy a very

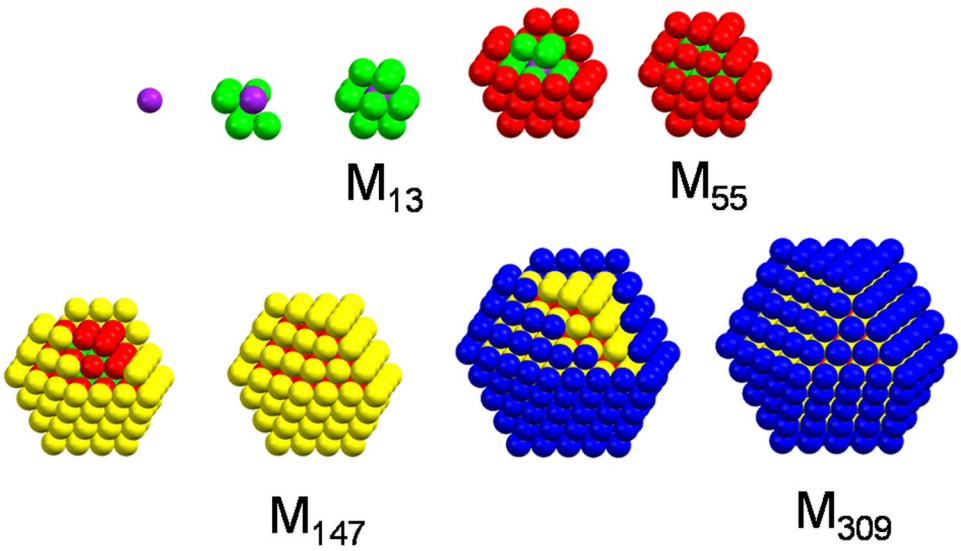

Fig. 5 Stepwise formation of full-shell clusters 13 (1 + 12), 55 (13 + 42) 147 (55 + 92) and 309 (147 + 162). Reprinted from ref. Schmid (2008) with permission from the Royal Society of Chemistry

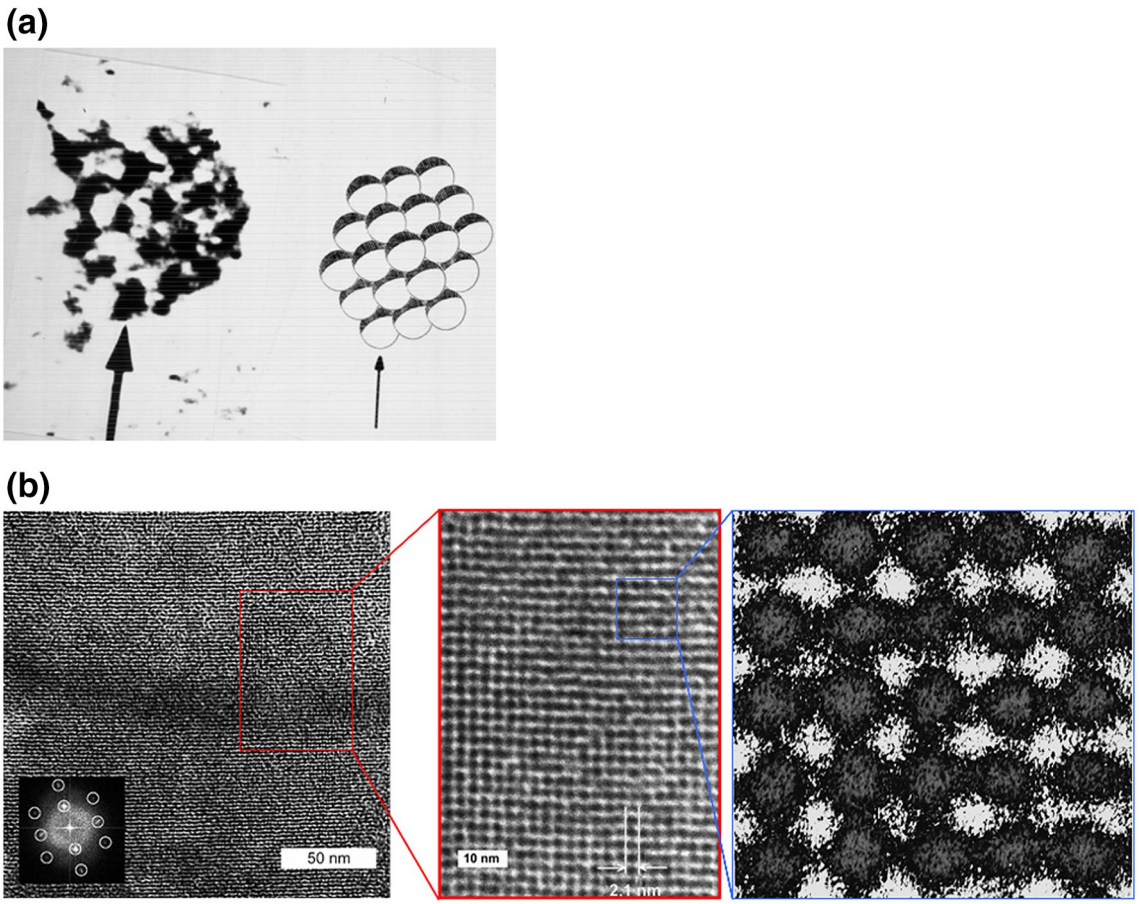

Fig. 6 TEM Image and sphere model of a Au_{55} core (**a**) and a monolayer of Au_{55} cores with magnified cutouts showing the monodispersity of the cluster (**b**). **a** Reprinted with permission from ref. Schmid (1992). Copyright (1992) American Chemical Society. **b** Reprinted with permission from ref. Schmid et al. (2000) from John Wiley and Sons

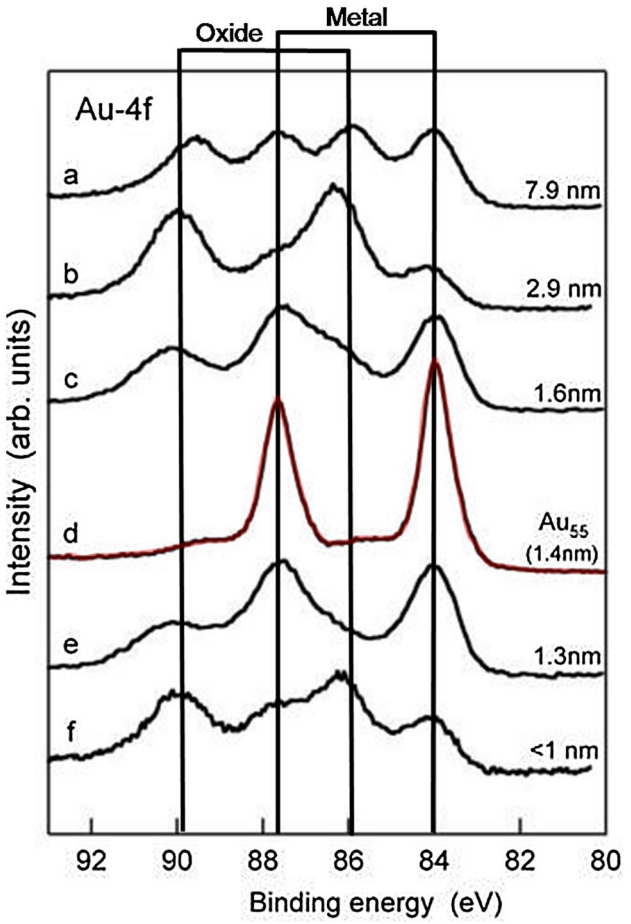

Fig. 7 Au-4f photoelectron spectra of different Au nanoparticles, treated in an oxygen plasma. All except Au_{55} show oxide signals. Reprinted from ref. Boyen et al. (2002) with permission from The American Association for the Advancement of Science

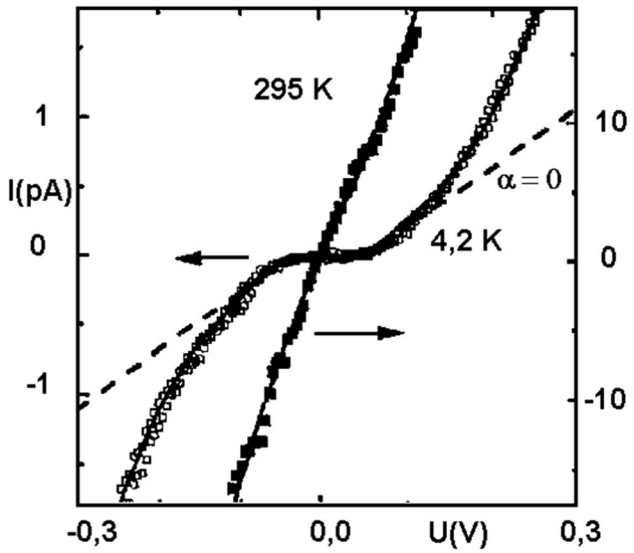

Fig. 8 Current (*I*)–voltage (*U*) characteristics of a 17 nm Pd particle at 295 and 4.2 K. Reprinted from Bezryadin et al. (1997) with the permission of AIP Publishing

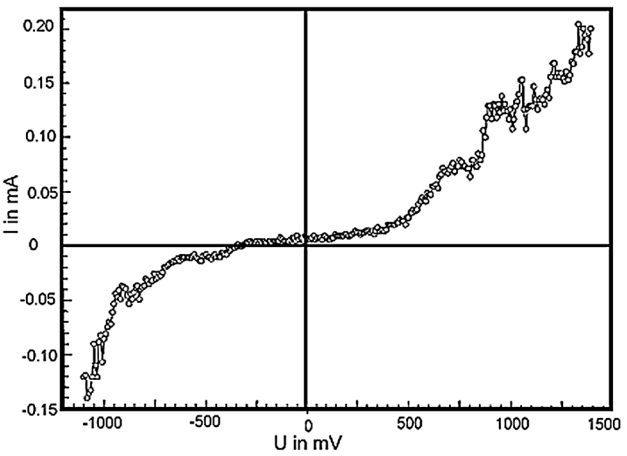

Fig. 9 *I–U* characteristic of $Au_{55}(PPh_3)_{12}Cl_6$ at room temperature indicating a well-expressed Coulomb blockade. With kind permission from Springer Science + Business Media: Chi et al. (1998)

special position in gold cluster chemistry which will be supported by many other results, especially in the field of cytotoxicity (see the following chapters).

Cytotoxicity and cellular uptake

The first study on cytotoxic effects of Au1.4MS in a series of human cancer cell lines was reported in 2005 (Tsoli et al. 2005). Eleven different cells lines were tested in comparison to Cisplatin (generic name for the trade name drug Platinol® and Platinol®-AQ), which is an established anticancer ("antineoplastic" or "cytotoxic") chemotherapy drug. These results are summarized in Table 1, which informs on the IC_{50} values of Cisplatin and Au1.4MS (here described an Au_{55}). In each case, Au1.4MS turned out to be comparable or even more toxic than Cisplatin, especially considering the difference in time to reach the respective IC_{50} values, i.e., 24 h for Au1.4MS and 72 h for Cisplatin.

These studies had been triggered by the previous findings that Au1.4MS strongly interacts with B-DNA, whereby it was observed that the ligand molecules, i.e., the weakly binding TPPMS ligands, are substituted by DNA sections comprising the major grooves. This was explained by the specific size conditions: the diameter of the cluster core is 1.4 nm and the height of the major groove in B-DNA is 1.3–1.5 nm. Supported by molecular calculations, it was concluded that there are strong chemical interactions between the Au_{55} core and the DNA due to the polydentate character of the major grooves (Liu et al. 2003). Therefore, some of the phosphine ligands need to be removed from

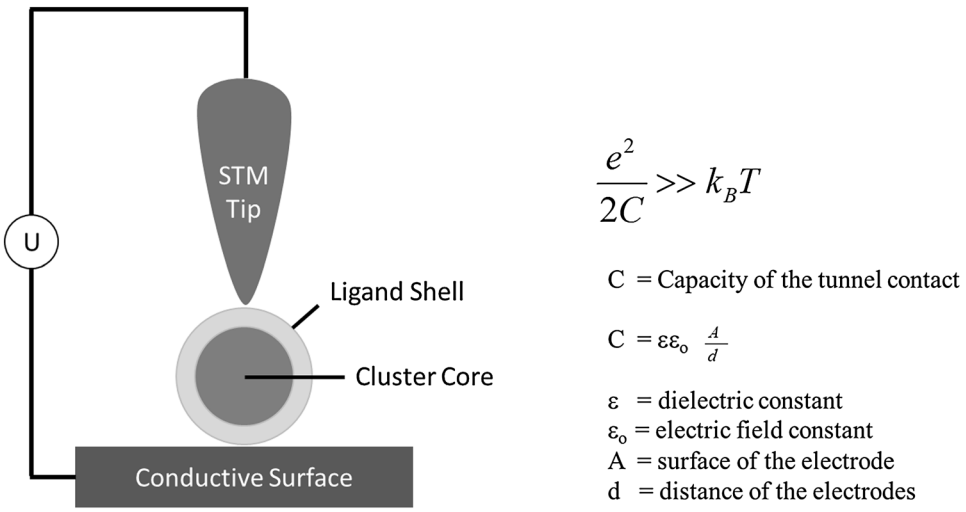

Fig. 10 Experimental setup to image and to investigate ligand protected nanoparticles by STM and Scanning Electron Spectroscopy (STS), respectively. The conditions to observe single electron transitions are that $e^2/2C \gg k_B T$ where $C = \varepsilon\varepsilon_o A/d$ is the capacity of the tunnel contact (ε_0 electric field constant, A surface of the electrode, d distance of the electrodes). Adapted from ref. Schmid (2008) with permission from the Royal Society of Chemistry

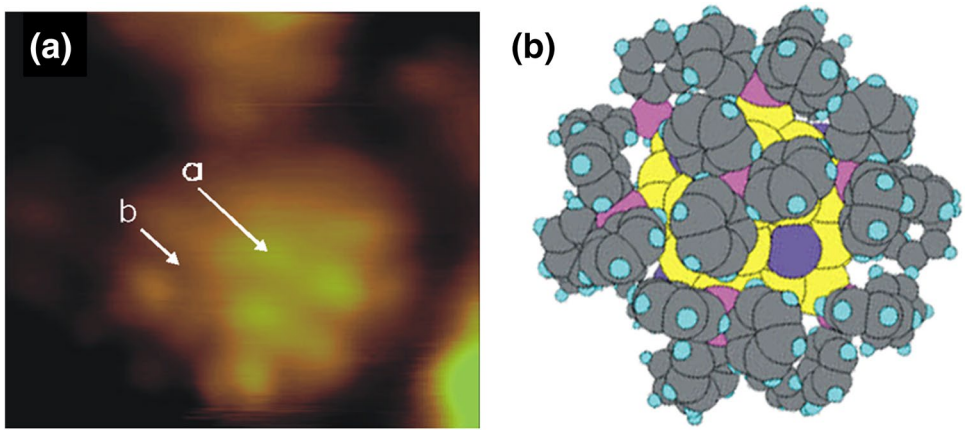

Fig. 11 **a** STM image of a single $Au_{55}(PPh_3)_{12}Cl_6$ cluster. The *light green areas* represent the electron rich phenyl rings of PPh_3. The positions *a* and *b* have been used to measure STS spectra (Zhang et al. 2003) (see Fig. 12). **b** Model of the cluster in the corresponding position. Reprinted from ref. Zhang et al. (2003) with permission from American Chemical Society

the original Au1.4MS, so that Au_{55} fits into the groove and, thereby, allows for interactions with electron-rich DNA components, i.e., the phosphate groups of the DNA backbone. The coverage of B-DNA with Au_{55} clusters has been visualized ex vivo by means of atomic force microscopy (AFM), after B-DNA was incubated with Au1.4MS in aqueous solution. Cross sections of the AFM image show the expected difference in height between unloaded and cluster-containing DNA sections. The observed 1.8 nm sections correspond with the sum of the DNA plus about half of the cluster, possibly still having some ligand molecules outside. Figure 14a shows the AFM image and the cross section indicating the difference between DNA with and without the 1.4 nm-sized AuNP, while Fig. 14b depicts the result of molecular modeling calculations that propose the binding of the cluster into the major groove.

These unexpected findings triggered a systematic study on the size-dependent cytotoxicity ranging from 0.8 to 15 nm with the cell lines HeLa, SK-Mel-28, L929, and J774A1 (Pan et al. 2007). Tauredon, a commercially available sodium aurothiomalate complex, being used for anti rheumatic treatment, has been applied as a reference. The results are illustrated in Fig. 15.

In accordance with the previous findings, for the 1.4 nm AuNP IC_{50} values ranging from 30 to 46 μM were obtained. Hence, this is the most toxic particle, as the IC_{50} values of the particles with 0.8 nm (Au_9 cluster, Gutrath et al. 2013), 1.2 and 1.8 nm were 250, 140, and 230 μM, respectively. These experiments also included reference measurements on pure ligands, as well as on a 1.4 nm sized AuNP with sodium 3,3′,3″-triphenylphosphine sulfonate (TPPTS) as ligand, which is the threefold sulfonated derivative of triphenylphosphine, thus being higher negatively charged, as compared to the monosulfonated TPPMS. These particles (labeled as Au1.4TPPTS in Fig. 16) showed similar IC_{50} values as Au1.4MS. In contrast, the 15 nm AuNPs were found to be non-toxic even at concentrations above 6300 μM than the smaller particles, indicating a clear trend of decreasing cytotoxicity with increasing particle size. Another interesting outcome of this study was that also the cellular response is size dependent, in that 1.4-nm particles cause predominantly rapid cell death by necrosis within

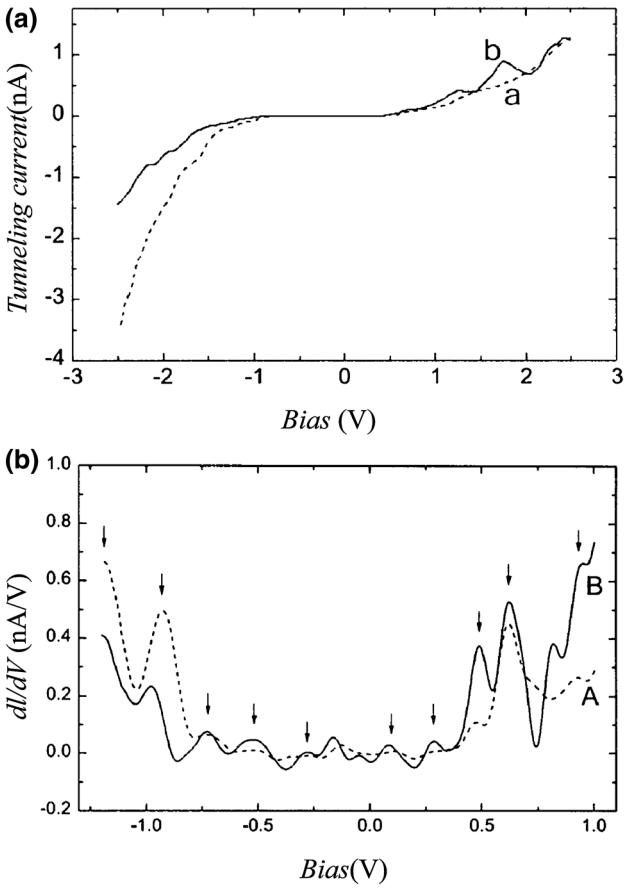

Fig. 12 **a** *I–U* characteristic of a single $Au_{55}(PPh_3)_{12}Cl_6$, measured at 7 K at two different positions. **b** d*I*/d*V* characteristic of the *curves a* and *b* indicating discrete energy levels with spacing of 170 mV. **a** Reprinted from ref. Schmid (2008) with permission from the Royal Society of Chemistry. **b** Reprinted from ref. Zhang et al. (2003) with permission from American Chemical Society

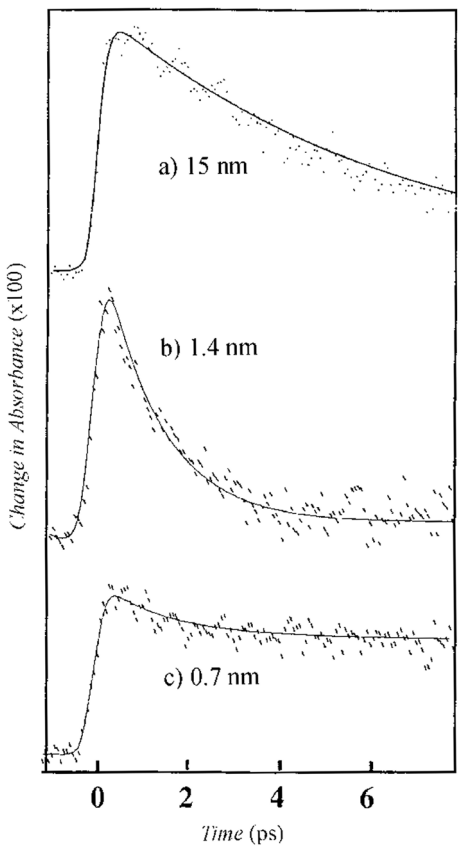

Fig. 13 The relaxation behavior of excited electrons of three AuNPs of different size. Reprinted from Smith et al. (1997) Copyright (1997), with permission from Elsevier

12 h, while closely related AuNP with 1.2 nm in diameter affects predominantly programmed cell death by apoptosis.

These data were complemented in a very recent study, which analyzed the cytotoxicity of AuNP in the size range between 1.4 and 15 nm, and thus fill the size gap between these two cornerstones of the highest and lowest cytotoxicity (Broda et al. 2016b). Besides Au1.4MS, AuNPs with 4.7, 10, 12, and 15 nm, all stabilized with either TPPMS or TPPTS, respectively, were tested regarding their cytotoxicity towards HeLa cells. Again, Au1.4MS was found to be the most cytotoxic species (IC_{50} value of 43 µM), while all other particles showed decreasing toxicity with increasing size up to 15 nm, which corroborates the clear trend of size-dependent cytotoxicity. Furthermore, these studies disclosed that all TPPTS-stabilized AuNPs were found to be less toxic than TPPMS-stabilized ones.

Pan et al. pointed out that for Au1.4MS and Au15MS, the major cell-death pathway is oxidative stress (Pan et al. 2009). All indicators of oxidative stress, reactive oxygen species (ROS), mitochondrial potential and integrity, and mitochondrial substrate reduction are compromised. In addition, they performed mRNA expression analysis using Affymetrix gene chips. The results are illustrated in Fig. 17. In a so-called heat map presentation, it is illustrated that a group of growth-related genes (PTGER4, EDN1, NR4A1, C5orf13, NR4A3, EGR3, FOS, EMP1, CALD1, SERPINE1, EGR1, DUSP5, ATF3, DUSP2) were upregulated in HeLa cells treated with both Au1.4MS (the signature of these particles is "s": small) and Au15MS (the signature of these particles is "b": big) at 1 h after the onset of treatment (s1h_1, s1h_2, b1h_1, b1h_2). This reflected an initial growth response triggered by addition of fresh media along with the Au1.4MS and Au15MS, which illustrates a well-known short-term phenomenon of cell culture and confirms the validity of the gene chip expression study. A separate clustering of the gene expression changes following treatment with the non-toxic Au15MS confirmed an overlapping, almost identical group of genes (EGR1, NR4A1, DUSP5, PPP1R3B, EDN1, FOS, EGR1, EDN1, ADAMTS1, ATF3, PTGER4, CYR61) as upregulated at 1 h after medium exchange irrespective of toxicity.

Table 1 IC_{50} values of 11 human cancer cell lines treated with Cisplatin for 72 h and with Au1.4MS (Au_{55}) for 24 h. Table adapted from Tsoli et al. (2005) with kind permission of John Wiley and Son

Cell line	IC_{50} cisplatin, 72 h (μM)	IC_{50} Au_{55}, 24 h (μM)
MC3T3-E1		
Bone cells	26.10 ± 1.27	1.65 ± 0.14
U-2OS		
Osteosarcoma	11.17 ± 2.02	0.64 ± 0.04
SK-ES-1		
Osteosarcoma	0.79 ± 0.17	1.03 ± 0.18
MOR/P		
Lung cancer cells	3.30 ± 0.30	2.10 ± 0.10
MOR/CPR		
Lung cancer cells	7.10 ± 1.2	2.50 ± 0.10
CCD-919Sk		
Fibroblast cells	0.45 ± 0.10	0.62 ± 0.07
BLM		
Metastatic melanoma	54.70 ± 7.60	0.30 ± 0.10
M V3		
Metastatic melanoma	>50	0.24 ± 0.02
SMel-28		
Melanoma	15.60 ± 2.26	1.12 ± 0.16
HeLa		
Cervical cancer cells	7.93 ± 0.95	2.29 ± 0.10
Hek-12		
Kidney cancer cells[a]	20.13 ± 6.0	0.63 ± 0.02

[a]Kidney cancer cells transformed with adenovirus

Following the initial growth response, heat shock and stress-related genes were upregulated after 6 h and strongly upregulated after 12 h in Au1.4MS-treated but not in Au15MS-treated or untreated HeLa cells. This group of genes (HSPA1A, DNAJA4, CHAC1, HSPA1A, DDIT3, GEM, LOC387763, PGF, HSPA6, SESN2, LOC284561, PPP1R15A, HMOX1, C16orf81, LOC344887, NGF, OSGIN1, FOSL1, CXCL2, IL8) suggested that a robust stress response had occurred in the Au1.4MS-treated cells. Highly elevated expression of heat shock proteins has been demonstrated to inhibit apoptosis at several stages including blocking of cytochrome c release from mitochondria, thus preventing the formation of an apoptosome and the activation of caspase-3, ultimately forcing cells into necrosis instead of apoptosis.

The gene expression profile in Au1.4MS is fully compatible with an oxidative stress response leading to necrosis. The previous studies of AuNP interaction with DNA suggested that the toxicity of Au1.4MS might be due to interference with DNA transcription. However, the strongly enhanced expression of 35 genes after exposure of HeLa cells to Au1.4MS and the continued expression of GAPDH both argued against direct transcriptional inhibition by Au1.4MS. This indicates that binding of the metal core of the Au1.4MS cannot be the sole or predominant reason for cytotoxicity. Nevertheless, a partial loss of the ligand shell being essential for the DNA binding is still considered as a precondition to unfold high AuNP cytotoxicity. This is confirmed by different experimental approaches:

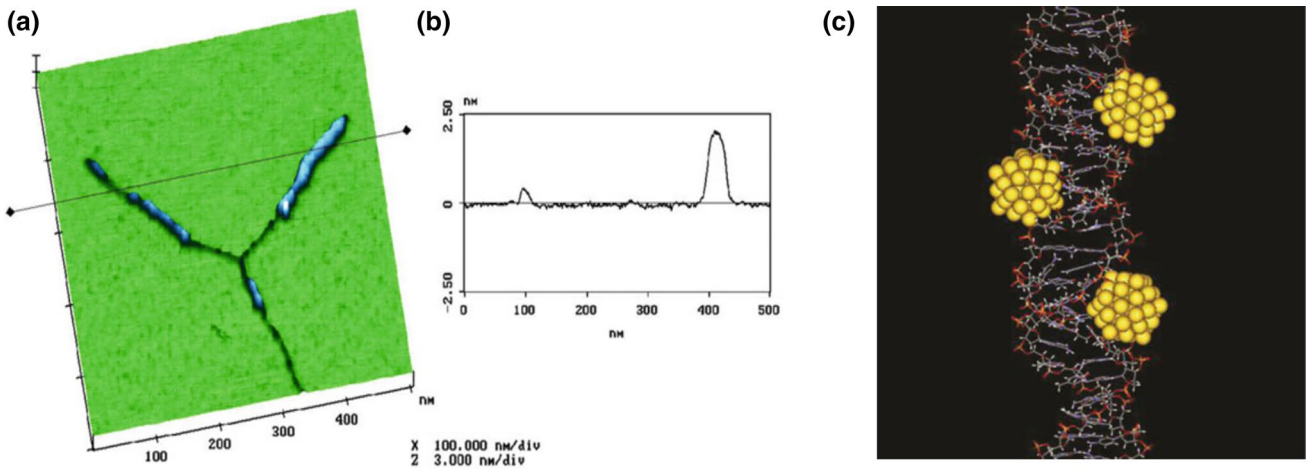

Fig. 14 **a** AFM image of DNA sections partially linked with Au_{55} clusters. **b** Height profile of unloaded and loaded parts, respectively. **c** Energy-minimized structure of B-DNA with Au_{55} clusters along the phosphate backbone of the major grooves. **b** Figure reprinted from Liu et al. (2003) with kind permission from John Wiley and Sons. **c** Figure reprinted from Tsoli et al. (2005) with kind permission from John Wiley and Sons

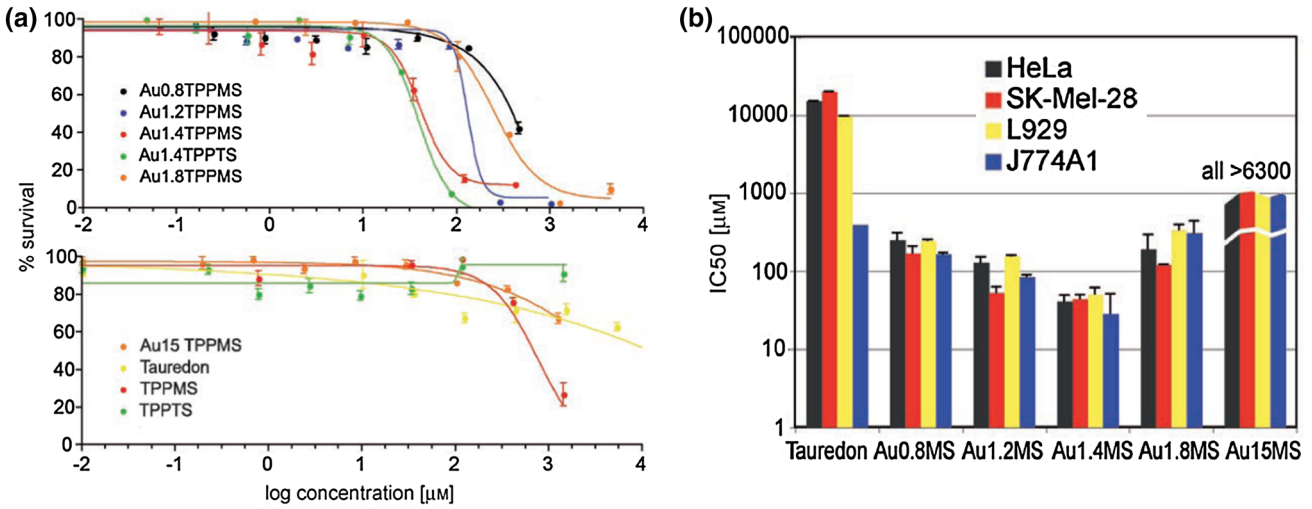

Fig. 15 Cytotoxicity of AuNP during the logarithmic growth phase of four cell lines. **a** HeLa cells were seeded at 2000 cells/well and grown for 3 days into the logarithmic growth phase. AuNPs were added for 48 h and MTT tests were performed. The logarithmic curve fits of tabulated MTT (3-(4,5-dimethylthiazol-2-yl)-2,5-diphenyltetrazolium bromide) readings are shown. Each data point represents the mean ± standard error (SE) of sample triplicates. **b** Note that the IC_{50} values of Au1. 4MS were lowest across all cell lines and that Au compounds of smaller or larger size were progressively less cytotoxic, which suggests a stringent size dependency of cytotoxicity. All concentrations relate to the amount of gold detected by atomic-absorption spectroscopy (AAS) in the authentic samples after performing the cytotoxicity test. This procedure ruled out the possibility that cluster synthesis contaminants or dilution errors may have caused erroneous results. Figure reprinted from Pan et al. (2007) with kind permission from John Wiley and Sons

The first one analyzes the effect of different reducing agents (RA) or antioxidants, i.e., *N*-acetylcysteine (NAC), glutathione (GSH), ascorbic acid (ASC) and TPPMS, comprising different binding affinities to the gold surface. The results are illustrated in Fig. 18. If the cells are pre-treated for 3 h with the respective RA, washed and post-treated with Au1.4MS, the cytotoxicity is unaffected. If either Au1.4MS was pre-treated with RA for 3 h and the mixture was added to the cells for 48 h, the cells were pre-treated with RA for 3 h, followed by the addition Au1.4MS and incubated for 48 h, or the RA was mixed with Au1.4MS and the mixture was immediately added to cells and incubated for 48 h; toxicity of Au1.4MS was significantly reduced, except for ascorbic acid. This led to the conclusion that the thiol-bearing molecules NAC and GSH as well as an excess of TPPMS stabilize the particles in solution, so that the unshielding of the bare gold core due to a partial loss of the ligand shell, which was anticipated as the precondition to unfold cytotoxicity, is prevented by the replacement of TPPMS with NAC or GSH or is effectively reduced by an excess of free TPPMS via the chemical equilibrium. This hypothesis was further confirmed by analyzing AuNPs of similar size (1.1 nm) that were directly capped with glutathione (Au1.1GSH) (Pan et al. 2009). These particles do not induce oxidative stress and, thus, are almost non-toxic.

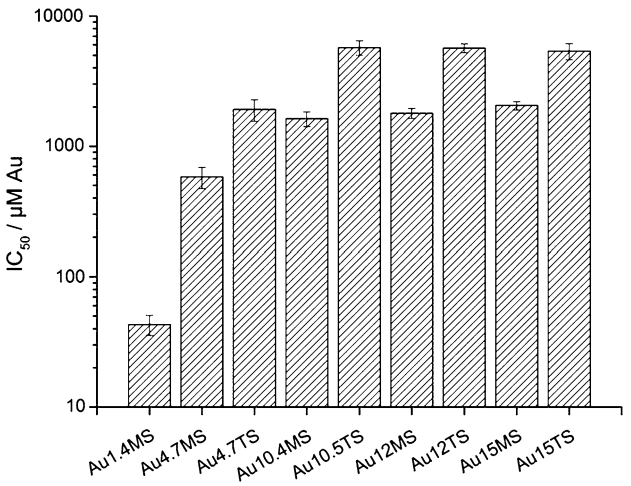

Fig. 16 IC_{50} values of different sized TPPMS- and TPPTS-stabilized AuNPs achieved from citrate-stabilized AuNPs. IC_{50} values are drawn in a logarithmic scale in given in µM Au. Therefore, a XTT (2,3-bis-(2-methoxy-4-nitro-5-sulfophenyl)-2*H*-tetrazolium-5-carboxanilide) vitality assay was applied by testing the cells during the logarithmic growth phase and determined the respective IC_{50} values. Reprinted from Broda et al. (2016b) Copyright (2016), with permission from Elsevier

The second approach utilized patch clamp measurements as a Food and Drug Administration (FDA)-established drug safety test (FDA 2005). Depending on the ligand composition, the 1.4 nm-diameter AuNP failed electrophysiology-based safety testing using human embryonic kidney cell line 293 cells expressing human ether-á-go–go-Related gene (hERG) (Leifert et al. 2013a). While the TPPMS-stabilized

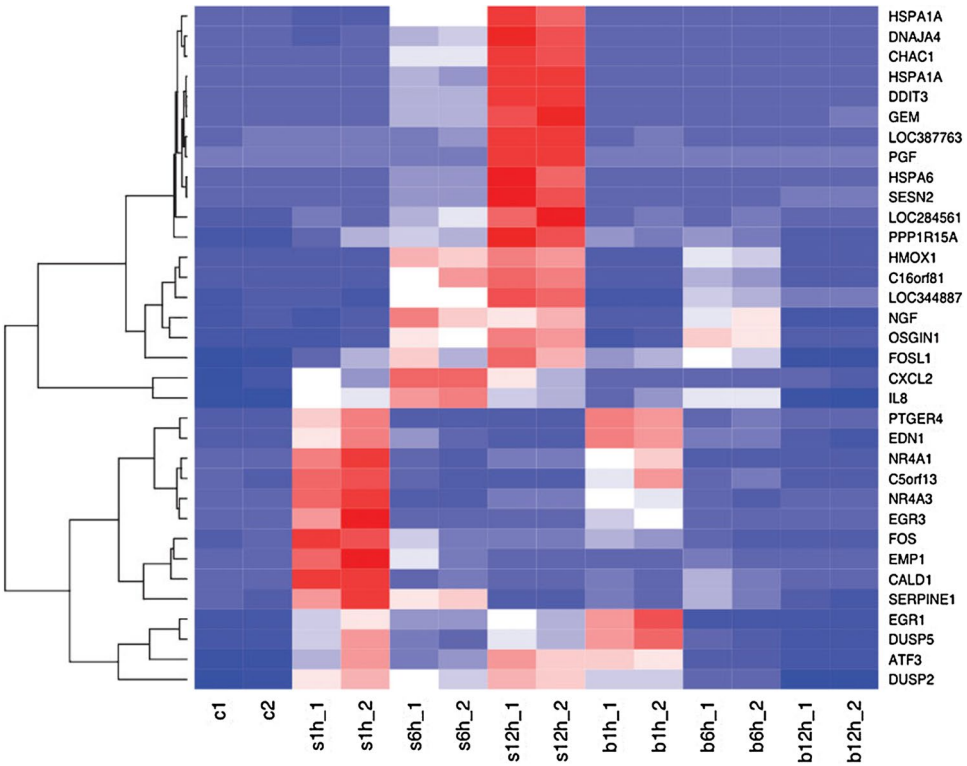

Fig. 17 Hierarchical cluster analysis and heat map representation of differentially regulated genes in AuNP-treated HeLa cells. All gene chip analyses were performed in duplicate (_1, _2). HeLa cells were left untreated (*c*) or were treated for 1, 6, and 12 h with Au1.4MS (s1 h–s12 h for small AuNPs) or with Au15MS (b1 h–b12 h for big AuNPs). Gene expression levels determined by Affymetrix gene chips were subjected to hierarchical cluster analysis. Upon treatment with Au1.4MS, 35 genes were significantly upregulated. Each gene is depicted by a single row of *colored boxes*. The *color* of the *respective box* in one row represents the expression value of the gene transcript in one sample compared with the median expression level of the gene's transcript for all samples shown. *Blue* transcript levels below median, *white* transcript levels equal to median, *red* transcript levels higher than median. Figure reprinted from Pan et al. (2009) with kind permission from John Wiley and Sons

AuNP irreversibly blocked hERG channels, GSH-stabilized AuNPs of similar size had no effect in vitro, and neither particle blocked the channel in vivo, which also holds the addition of excess TPPMS (see Fig. 19). The blockade of the hERG channel by Au1.4MS was irreversible and control experiments confirmed that it is not caused by the ligand TPPMS, which exhibited a reversible blockade, and only at very high concentrations. This confirms that the binding modality between metal and ligand is a relevant parameter; hence, the shielding of the AuNP surface plays a crucial role in the cytotoxicity of Au1.4MS. These findings were supported by docking simulation of AuNPs, carrying a varying number of ligands in contact with the hERG channel, suggesting a differential interaction facilitated by the complementarity in size and shape.

Cellular uptake and distribution

As pointed out before, the physico-chemical properties of inorganic nanoparticles, in general, depend on the intrinsic properties of the particle core as well as on the composition of the ligand shell (Dreaden et al. 2012). These ligands have several functions. Most important, they increase the colloidal stability of the particles in biological environments by steric or electrostatic means. Furthermore, they are thought to enhance the biocompatibility of the inorganic NPs. Hence, the short- and long-term stability of the ligand shell is of vital importance for the evaluation of the bioactivity and fate of the particles in vivo. This does not only hold for weakly binding ligands, such as phosphines on gold. A recent study has demonstrated that even firmly grafted polymer shells around 5 nm AuNPs, bound to the gold core via thiol terminated, strongly binding anchor groups, may degrade within 24 h when injected into rats (Kreyling et al. 2015). The findings discussed above indicate the need of detailed investigations on the intracellular integrity of the cytotoxic 1.4 nm-sized AuNP. Although it is most likely that nanoparticle toxicity follows endocytosis, it is entirely possible that the toxicity may stem from interactions at the cell membrane, even though the particles are also endocytosed (Broda et al. 2016a). However, the

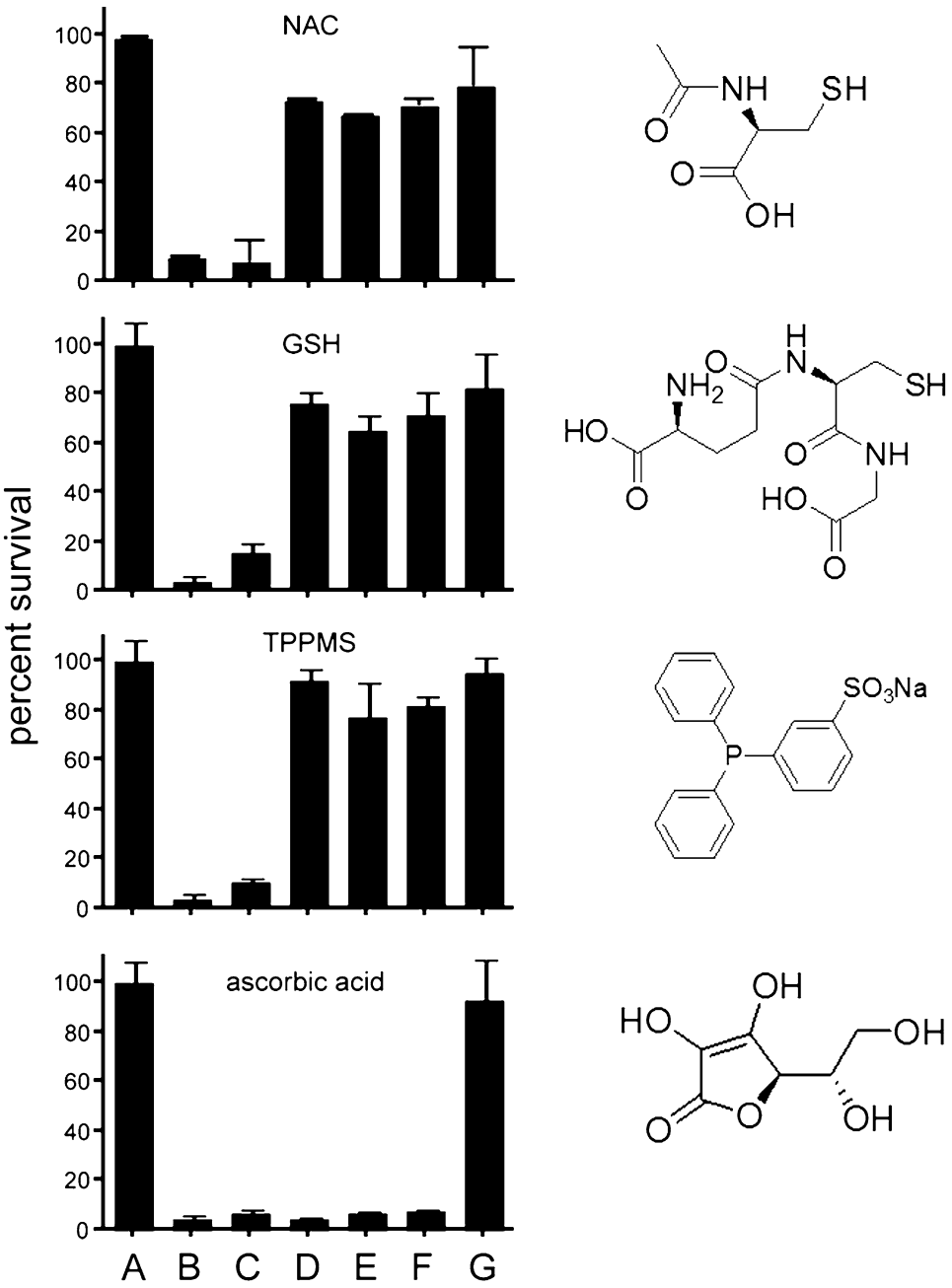

Fig. 18 Bar chart and the corresponding molecular structures of RA rested. NAC, GSH, and TPPMS but not ascorbic acid can partially inhibit the cytotoxicity of 100 mM Au1.4MS. *A* Untreated cells. *B* Cells treated with Au1.4MS for 48 h. *C* Cells pre-treated with reducing agent for 3 h, washed, and post-treated with Au1.4MS for 48 h. *D* Au1.4MS pre-treated with reducing agent for 3 h, and mixture added to cells for 48 h. *E* Cells pre-treated with reducing agent for 3 h, then Au1.4MS added and incubated for 48 h. *F* Reducing agent mixed with Au1.4MS and mixture immediately added to cells and incubated for 48 h. *G* Cells incubated with reducing agent for 48 h. Figure reprinted from Pan et al. (2009) with kind permission from John Wiley and Sons

specific binding situation of the ligand shell in Au1.4MS may also promote direct penetration of the cell membrane, which is consistent with recent studies on the interaction of Au1.4MS with model membranes (Broda et al. 2016b).

The localization of inorganic NP in cells can be analyzed by means of transmission electron microscopy. However, imaging of inorganic NP, in particular in the sub-2 nm range, is still a big technical challenge due to resolution limitations on biological media, caused, e.g., by inelastic scattering or high electron beam sensitivity of the biological material (He et al. 2007; Marquis et al. 2009; Sousa et al. 2012). Alternatively, AuNP in this size range can be traced in biological samples using either nuclear radiation detection or fluorescence detection (for the ligand shell, if equipped with a fluorescence marker).

For nuclear radiation detection, the isotope ^{197}Au, which is both a mononucleidic and monoisotopic element, is transferred into the radioactive isotope ^{198}Au by means of neutron activation (^{197}Au (n, γ) ^{198}Au), which allows for quantitative detection of Au in the biological samples. This analytical method is called neutron activation analysis, NAA. However, NAA is rather limited in spatial resolution so that

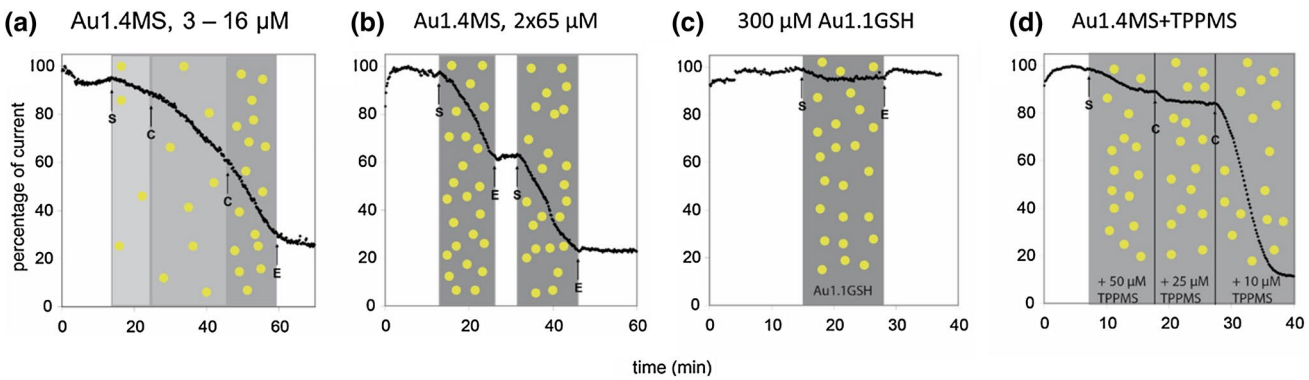

Fig. 19 Patch-clamp measurement of hERG tail current peak amplitudes in HEK 293 cells stably expressing the hERG ion channel. **a** Concentration-dependent inhibition of hERG current by Au1.4MS (3.1, 6.5, and 16.25 µM gold atom concentrations), sequentially applied to the same cell. The *shaded areas* indicate the intervals of different compound concentrations [Au] and [TPPMS], respectively. After a latency time of typically 2–3 min, an increase in the slope of current decay with increasing Au1.4MS concentration is observed. *Arrows* indicate start (S), change (C), and end (E) of perfusion with the differently concentrated AuNP solutions. **b** Inhibition of hERG current by 65 µM Au1.4MS shows no recovery upon washout. *Arrows* indicate start (S) and end (E) of perfusion with AuNP solution. The blocking of the hERG channel by Au1.4MS is irreversible and additive. **c** Application of 300 µM Au1.1GSH did not affect the hERG current. The *shaded areas* indicate the intervals of different compound concentrations of [Au] in Au1.1GSH. **d** Pre-incubation of Au1.4MS with different concentrations of TPPMS abolished the hERG blocking potency of 20 µM Au1.4MS when TPPMS was present in excess. The cell was perfused with a mixture of 20 µM Au1.4MS + 50 µM TPPMS, 20 µM Au1.4MS + 25 µM TPPMS, and 20 µM Au1.4MS + 10 µM TPPMS. Reprinted from Leifert et al. (2013a, b) with kind permission of PNAS

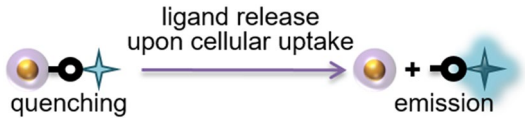

Fig. 20 Cytotoxic 1.4 nm-sized AuNPs are functionalized with a fluorophore Cascade Blue Ethylenediamine®. In this state the fluorescence emission of the CBE is quenched. By ligand release upon cellular uptake, fluorescence reappears and gets visible in the fluorescence images of HepG2 cells (see Fig. 21). Figure reprinted from Broda et al. (2016a) with kind permission from John Wiley and Sons

quantification of gold is not feasible on a single cell level but requires integration over a larger number of cells. In contrast, ligand shell of AuNPs may directly be traced on the cellular level by utilizing fluorescence quenching (Ke et al. 2014) and/or enhancing effects (Chowdhury et al. 2006). To investigate the hypothesized ligand loss of Au1.4MS upon cellular uptake, new phosphine-stabilized cytotoxic Au1.4MS has been synthesized bearing a fluorophore, so that fluorescence dequenching can be utilized to visualize the fate of the ligand.

Broda et al. introduced a new type of cytotoxic 1.4 nm-sized AuNP, where the gold core is functionalized with a fluorophore Cascade Blue Ethylenediamine® (CBE), described as Au1.4MS/CBE (Broda et al. 2016a). Upon binding of the fluorophore covalently to the AuNP-surface, the fluorescence emission of the CBE is quenched. However, fluorescence reappears as soon as it is released from the AuNP's surface (cf. Fig. 20).

To investigate the subcellular distribution of CBE, HepG2 cells, we treated with 100 µM of Au1.4MS/CBE. Although cytotoxic effects have been observed, in cells with overall healthy morphology CBE molecules were found to be homogenously distributed over the cytoplasm and concentrated to some extent at the cell membrane (Fig. 21a). Moreover, fluorescence was found inside the nucleus, however, with lower intensity compared to the cytosol. The results led to the conclusion that at least a fraction of CBE is no longer covalently attached to the AuNP's surface (Broda et al. 2016a). The released CBE was furthermore able to enter the cell as well as the nucleus and could be found in various subcellular compartments including cytosol, nucleus and plasma membrane. However, from the localization of released fluorophores alone, it could neither be concluded where the detachment occurred nor could be deduced that Au1.4MS/CBE has been taken up by the cells. To prove the uptake Au1.4MS, irrespective of whether still bound to CBE or not, NAA on cell fractionations was carried out after exposure of HepG2 cells to AuNPs.

In cells which were incubated with 75 µM AuNP solutions of Au1.4MS and Au1.4MS/CBE, respectively, (339 ± 20) ng Au stemming from Au1.4MS and (569 ± 113) ng Au stemming from Au1.4MS/CBE were found in the cytosolic fractions (Fig. 21b). In contrast to previous studies (Verma and Stellacci 2010), only low amounts of gold were found in the nuclear fractions. The distribution of the incorporated AuNPs in the cytosolic and nuclear fraction is 96.6–3.4 and 95.2–4.8% for Au1.4MS and Au1.4MS/CBE, respectively. The differentiation between membrane-bound and incorporated AuNPs

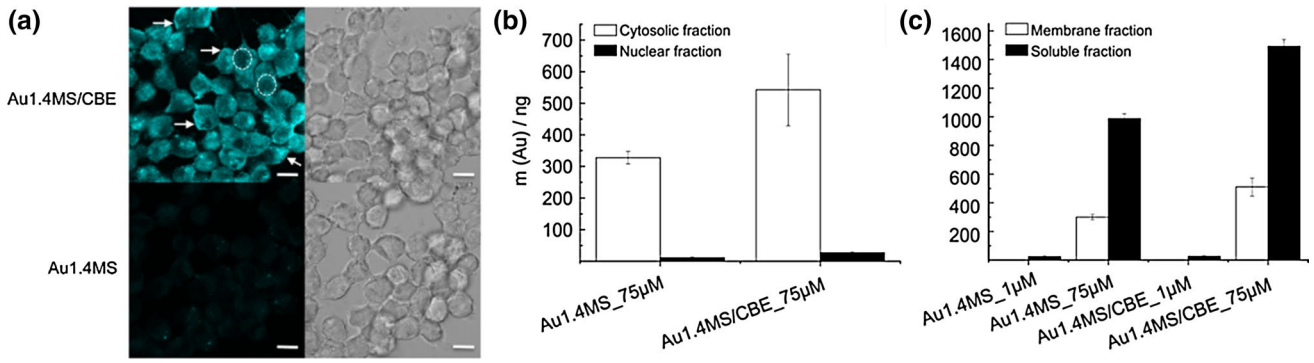

Fig. 21 **a** CLSM images of HepG2 cells incubated for 20 h with 100 µM Au1.4MS/CBE or 100 µM Au1.4MS as indicated. Fluorescence (*left*) and bright-field images (*right*) are shown. *Arrows* point to increased fluorescence at the cell membrane. Nuclei appear with lower fluorescence as exemplified with *dotted circles*. *Scale bars* represent 10 µm. **b**, **c** Gold amounts determined via NAA for **b** cytosolic and nuclear fractions and **c** for membrane and soluble fractions. HepG2 cells were incubated for 24 h with 1 µM and 75 µM Au1.4MS or Au1.4MS/CBE. Figure reprinted from Broda et al. (2016a) with kind permission from John Wiley and Sons

Table 2 Internalized AuNPs per cell and cellular uptake efficiencies of HepG2 cells incubated 24 h with 1 and 75 µM Au1.4MS or Au1.4MS/CBE determined by referring the applied gold concentration to the sum of the gold amount found in the soluble and the membrane fractions. Table reprinted from Broda et al. (2016a) with kind permission from John Wiley and Sons

Sample	Applied Au concentration (µM)	Internalized AuNPs per cell	Cellular uptake efficiency/%
Au1.4MS	1	1.9×10^5	2.5
Au1.4MS	75	9.5×10^6	1.7
Au1.4MS/CBE	1	1.9×10^5	2.7
Au1.4MS/CBE	75	1.5×10^7	2.7

revealed membrane association of a substantial portion of both Au1.4MS and Au1.4MS/CBE (Fig. 21c). This is a priori surprising, as the particles are negatively charged and are thus not expected to be attached to the negatively charge cell membrane. However, membrane-bound negatively charge AuNPs may be bound non-specifically to cationic patches on the otherwise negatively charged membrane (Schaeublin et al. 2011). The difference in overall lower gold amount detected is attributed to different procedure in cell fractionation.

The cellular uptake efficiency was derived from the sum of the detected gold amount in the soluble and the membrane fractions related to the applied gold amount. In accordance with the previously reported data (Soenen et al. 2012; Alkilany and Murphy 2010), the cellular uptake efficiency is 2–3%, which corresponds to approx. 105–107 particles per cell (see Table 2). A generally higher uptake is reported for positively charged AuNPs (Alkilany and Murphy 2010; Bogart et al. 2014).

The data show that Au1.4MS/CBE was more efficiently taken up than Au1.4MS, although they exhibit a higher negative surface charge due to the three sulfonate groups per CBE group. The authors point out that this is in line with the previously reported increased internalization of 1.5 nm-sized negatively charged AuNPs into HaCaT cells compared to cationic and neutral ones (Soenen et al. 2012). This is attributed to the adsorption of serum proteins from the cell culture media, which could induce the entry of AuNPs into cells by receptor-mediated endocytosis (Rivera-Gil et al. 2013; Rosi et al. 2006). However, even if serum proteins are adsorbed onto the AuNPs' surface the effect on the cytotoxic properties is negligible as both particle species exhibit similar IC_{50} values. This confirms the hypothesis that the partial or complete loss of the TPPMS ligand shell, to which serum proteins will bind, is a prerequisite to unfold the cytotoxicity of these usAuNP.

In vivo toxicity tested in zebrafish embryo essays

As pointed out in many works, the zebrafish embryo tests (FET) are considered suited as a complex vertebrate test to study the toxicity of nanoparticles (Scholz et al. 2008; Kosmehl et al. 2012). 25% of the zebrafish genes are known to be essential for early development and 99% of these genes are homologous to human genes (Amsterdam et al. 2004). This suggests that results obtained in zebrafish may be transferable to humans. Anyway, they are highly useful for 'intermediate' toxicity testing, after completing initial experiments in cells, and before turning to in vivo experiments in rodents (Rizzo et al. 2013).

Jahnen-Dechent and coworkers recently showed that FET reproduced all important findings of a previous study in HeLa cells concerning the toxicity effects of Au1.4MS, as discussed above, and added new important information on teratogenicity and hepatotoxicity that could not

be gained from studying cultured cells (Pan et al. 2013). They compared Au1.4MS and equally sized Au1.4GSH, where GSH stands for glutathione. In their study, Au1.4MS caused embryo coagulation at the lethal dose of 400 mM. At a sub-lethal dose of 50 mM, Au1.4MS caused hypopigmentation and pericardial edema. The malformations were absent in embryos exposed to Au1.4GSH at an even higher dose (1 mM) and, in accordance with the cytotoxicity test in HeLa cells, the toxicity of Au1.4MS was drastically reduced, when GSH was added.

Antibacterial effects

To explore the potential therapeutic activity of cytotoxic usAuNP, Boda et al. investigated treatment option against staphylococcal infections (Boda et al. 2015). The emergence of multidrug resistant bacteria, especially biofilm-associated Staphylococci, requires novel antimicrobial agents. The authors tested antibacterial activity of AuNPs in a size range between 0.8 and 10 nm against planktonic Gram-positive and Gram-negative pathogenic bacteria. Among the Gram-positive strains, *Staphylococcus aureus* and *S. epidermidis* were tested, while *Escherichia coli* and *Pseudomonas aeruginosa* comprised the Gram-negative strains. In concentration-dependent toxicity assessment, the minimum inhibitory concentration (MIC) and minimum bactericidal concentration (MBC) were evaluated. The results are summarized in Table 3.

They found that usAuNPs with core diameters of 0.8 and 1.4 nm, i.e., Au0.8MS and Au1.4MS, both being stabilized with TPPMS, both have minimum inhibitory concentration (MIC) and minimum bactericidal concentration of 25×10^{-6} M [Au]. However, in contrast to the previously discussed cytotoxicity data, the bactericidal activity of Au0.8MS was found to be higher than for Au1.4MS. In accordance with all previous findings, thiol-stabilized AuNP [in this study, AuNP with diameter of 1.9 nm (AuroVist) were used] did not cause significant toxicity in any of the bacterial strains.

In kill kinetics studies, where Au0.8MS and Au1.4MS were studied at their MIC in staphylococci, both particles caused acute toxicity in *S. aureus* and *S. epidermidis*, respectively. Thereby, an up to 5 $\log_{10}$ reduction in viable bacteria was measured within 5 h of exposure. As can be seen in Fig. 22, between 5 and 21 h, bacterial growth resumed due to the growth of resistant bacteria with the exception of Au0.8MS-treated *S. aureus*. This specific test did not show signs of recovery even after 24 h of culture.

Although, no explanation of the superior antibacterial properties of Au0.8MS is explained, yet the results document antibacterial effects of TPPMS-stabilized usAuNP below the IC_{50} concentrations reported for eukaryotic cells. This suggests a therapeutic window for such particles below host toxic concentrations.

Biodistribution and pharmacokinetics

To determine accumulated fractions in secondary organs and tissues, the ultimate aim is to quantitatively balance the fractions of NP in all relevant organs and tissues of the body and include the remaining body and total excretion collected between application and analysis as a function of retention time, i.e., quantitatively balanced biokinetics of the incorporated AuNP as described earlier (Kreyling et al. 2013; Geiser and Kreyling 2010). Note that the selective

Table 3 Summary of (A) MIC and (B) MBC of TPPMS-stabilized AuNP against different bacterial strains

	E. coli	*S. aureus*	*S. epidermidis*	*P. aeruginosa*
(A) Minimum inhibitory concentration (MIC) in $\times 10^{-6}$ m				
Au0.8MS	No inhibition	25	25	No inhibition
Au1.4MS	No inhibition	25	25	≥400
Au5.1MS	≥400	≥400	≥400	≥400
Au8.7MS	≥400	≥400	≥400	No inhibition
Au10.4MS	≥400	≥400	≥400	No inhibition
AuroVist	No inhibition	No inhibition	No inhibition	≥400
(B) Minimum bactericidal concentration (MBC) in $\times 10^{-6}$ m				
Au0.8MS	ND	25	25	ND
Au1.4MS	ND	25	25	ND

The MIC and MBC values denoted above correspond to a minimum of four concordant experimental values obtained among 4–6 replicates

ND not determined

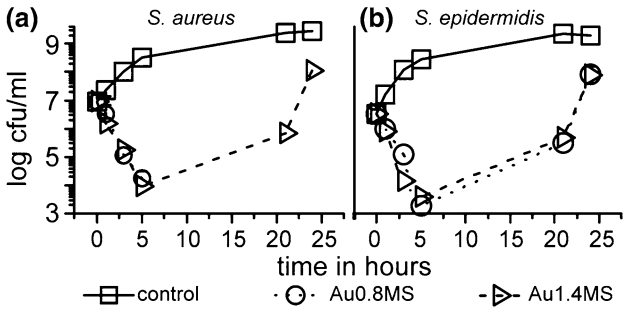

Fig. 22 Growth kinetics of **a** *S. aureus* and **b** *S. epidermidis* exposed to Au0.8MS and Au1.4MS at MIC (25×10^{-6} M Au) for 0–24 h, presented by the number of colony forming units per mL (cfu/mL). Figure reprinted from Boda et al. (2015) with kind permission from John Wiley and Sons

analyses of selected organs may cause substantial uncertainty of the fate of incorporated AuNP.

Size-dependent biokinetics after three routes of application

For a systematic attempt of the effect of the AuNP size, we used a suite of monodisperse AuNP ranging from 1.4 via 5, 18, and 80 to 200 nm all surface-modified with TPPMS resulting in a negative zeta-potential and, additionally, 2.8 nm AuNP either coated with thioglycolic acid (TGA) exhibiting a terminal carboxyl group ($–COO^-$) or with cysteamine group exhibiting a terminal amino group ($–NH_3^+$) achieving either a negative or a positive zeta-potential. These AuNPs were applied to healthy, adult female rats via three routes [intratracheal (IT) instillation, oral ingestion by gavage and intravenous tail-vein (IV) injection] to directly compare the effect caused by different organs of intake—lungs versus gastrointestinal-tract (GIT) versus systemic circulation in blood (Kreyling et al. 2014; Schleh et al. 2012; Hirn et al. 2011; Semmler-Behnke et al. 2008).

All AuNPs were radioactively labeled by neutron irradiation in a nuclear research reactor (^{197}Au (n, γ) ^{198}Au) prior to use as described previously (Kreyling et al. 2014; Schleh et al. 2012; Hirn et al. 2011; Semmler-Behnke et al. 2008). Physicochemical parameters of the AuNP including specific ^{198}Au radioactivity and the isotope ratio of ^{198}Au to stable ^{197}Au are given in the previous reports. Due to the short radioactive half-life of ^{198}Au (2.7 days), biodistributions were quantitatively determined up to three times within the first 24 h after application.

Figure 23 shows that IT-instilled AuNPs were retained predominantly in the lungs including small but size-dependent AuNP translocations towards blood circulation and subsequent accumulation in all secondary organs and tissues (left panel); in contrast, more than 95% of the gavaged AuNPs were passing through the GIT for fecal excretion including even smaller but also size-dependent fractions of absorbed AuNP through the GIT-epithelia towards blood circulation and subsequent accumulation in secondary organs and tissues (middle panel). In further contrast, after IV-injection AuNPs were rapidly cleared from circulation within 1 h in a size-dependent manner and predominantly accumulated in liver (right panel) followed by spleen and other secondary organs as well as tissues (Fig. 24).

Figure 24 compares the accumulation of 18 nm AuNP between 1 and 24 h in secondary organs and tissues after all three applications—IT-instillation, Gavage and IV-injection. To compare accumulation in secondary organs and tissues directly between the three application routes, fractions of the initially applied dose after IV-injection are compared with fractions relative to the amount of AuNP which had entered blood circulation for subsequent accumulation after crossing the ABB or the GIT-epithelium, respectively. It is remarkable how rapid accumulation had occurred already 1 h after application; further accumulation until 24 h is rather modest in

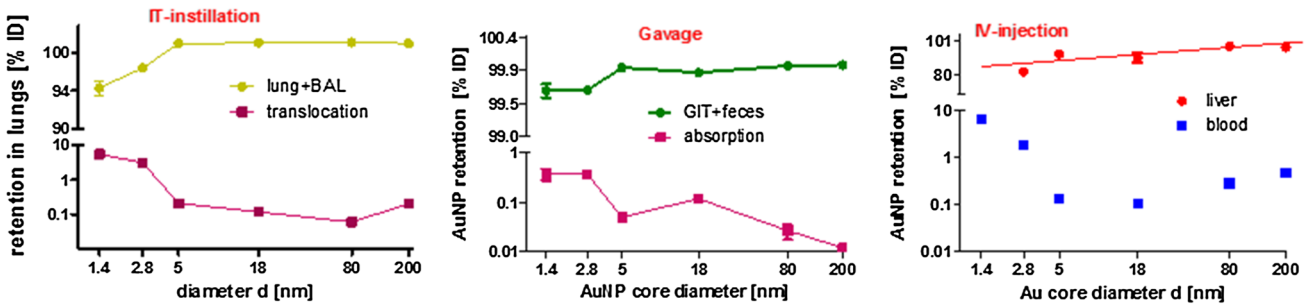

Fig. 23 Size dependent 24 h retentions AuNP in organs of intake (i.e., lungs, GIT, blood) as percentage of initially applied dose (ID) after all three AuNP applications. In addition, total translocation across the air-blood-barrier (ABB) and absorption across the GIT epithelium are shown after IT-instillation and gavage, respectively; and the dominant liver accumulation after IV-injection (Kreyling et al. 2014; Schleh et al. 2012; Hirn et al. 2011; Semmler-Behnke et al. 2008). Mean data ± SEM of $n = 4$ rats for each AuNP size. Note that the AuNPs tested are TPPMS stabilized except the 2.8 nm AuNP, which are stabilized with TGA exhibiting a terminal carboxyl group

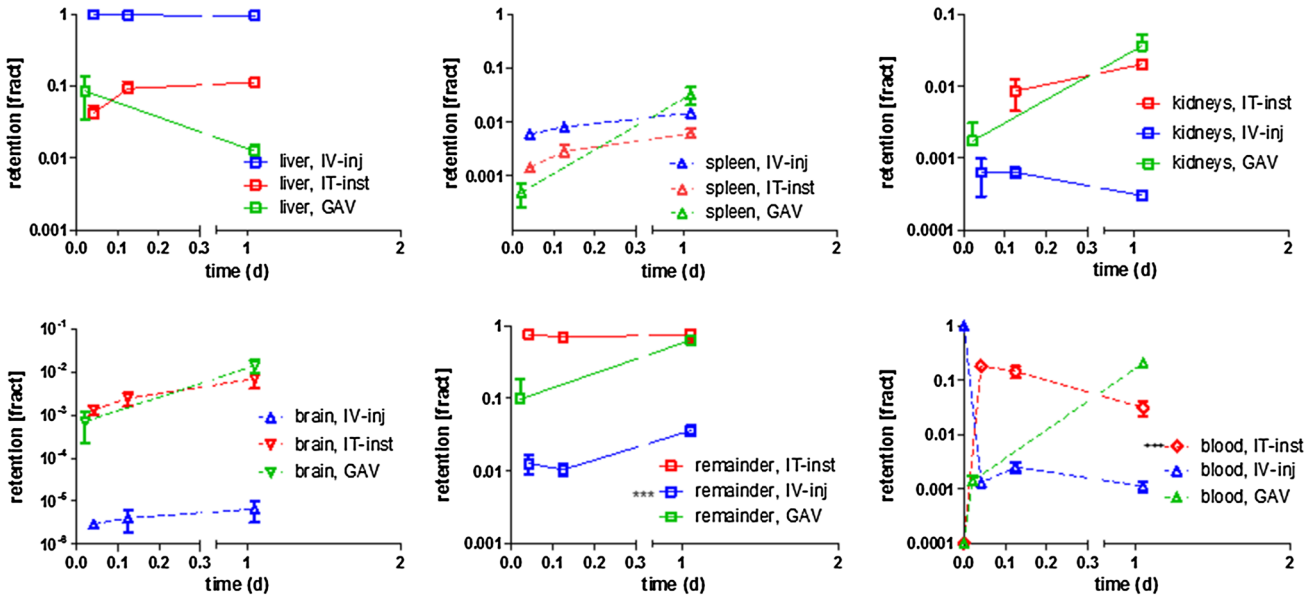

Fig. 24 Biokinetics patterns of Au18MS between one and 24 h after IT-instillation, gavage or IV-injection in liver, spleen, kidneys (*upper panels*) and in brain, remaining carcass and blood (*lower panels*). IV-injection fractions are relative to ID; fractions of IT-instillation or gavage are normalized to the AuNP fraction which had crossed the ABB or GIT-epithelium, respectively, into circulation for subsequent accumulation. Note, in all organs and the carcass the AuNP content in the residual blood volume of each organ was estimated and subtracted; therefore, the data present AuNP retained in the tissues of each organ. Mean ± SEM, $n = 4$ rats for each time point

all secondary organs and the remaining carcass after IT-instillation or IV-injection, respectively. However, after gavage AuNP accumulation increases more than tenfold in spleen, kidneys, brain and carcass while in liver the AuNP content declines an order of magnitude after 1 h. In blood, freshly IV-injected AuNP decreased a 1000-fold within 1 h and stayed constant at this low level during the next 24 h. None of the clearance mechanisms are fully understood but it appears that liver macrophages (Kupffer cells) effectively and rapidly catch more than 90% of the circulating AuNP after IV-injection while only about 1% AuNP is retained in both spleen and carcass and even lower fractions are found in other organs. In contrast, of those AuNPs which had crossed the ABB after IT-instillation, the blood fraction is higher than 10% at 1 h and declines gradually. AuNP fractions of about 10% in the liver are as high as in blood and increase slightly over time. A similar gradual increase is seen in the other secondary organs although on a lower level. Note that the highest content of translocated AuNP (>80%) is found in the carcass comprising the skeleton, muscles, fat, skin, etc.

After gavage AuNP patterns are again different to those after IV-injection or IT-instillation; of those AuNPs which had crossed the GIT-epithelium, the AuNP fraction in blood is only 0.1% but increases drastically a 100-fold during the next 24 h. Since in most organs and the carcass AuNP contents increase between tenfold and 100-fold, it appears plausible that the passage across the GIT-epithelium into blood occurs in a prolonged fashion compared to ABB translocation. 10% of the circulating AuNPs is rapidly removed by the liver but a tenth of those AuNPs escape the liver and become again redistributed in the organism.

The large differences in the biokinetics patterns of the identical AuNP after the three routes of application clearly indicate that after each application the AuNPs interact differently with the constituents of the circulating blood and the vascular membranes of the secondary organs and tissues although each AuNP size of this set of monodisperse of AuNP was dispersed in the same suspension. Note however, two major differences between IV-injection versus IT-instillation or gavage are the AuNP dose and dose rate in blood circulation, although the applied AuNP doses were the same at all three applications. But during IV-injection, the AuNP suspension is injected as a bolus into the tail vein within 20–30 s while after IT-instillation and after gavage the crossing of the ABB or GIT-epithelium, respectively, is prolonged over the first few hours and the amount of AuNP which crossed either membrane is 2–3 orders of magnitude lower than after IV-injection. Even the contributions of pathways across either membrane are unclear: after IT-instillation, AuNPs were found in endothelial cells of alveolar vascular vesicles (Geiser and Kreyling 2010) but AuNP may well enter lymphatic drainage before entering circulation which will likely take more time than just crossing through vascular endothelial cells. There are doubts

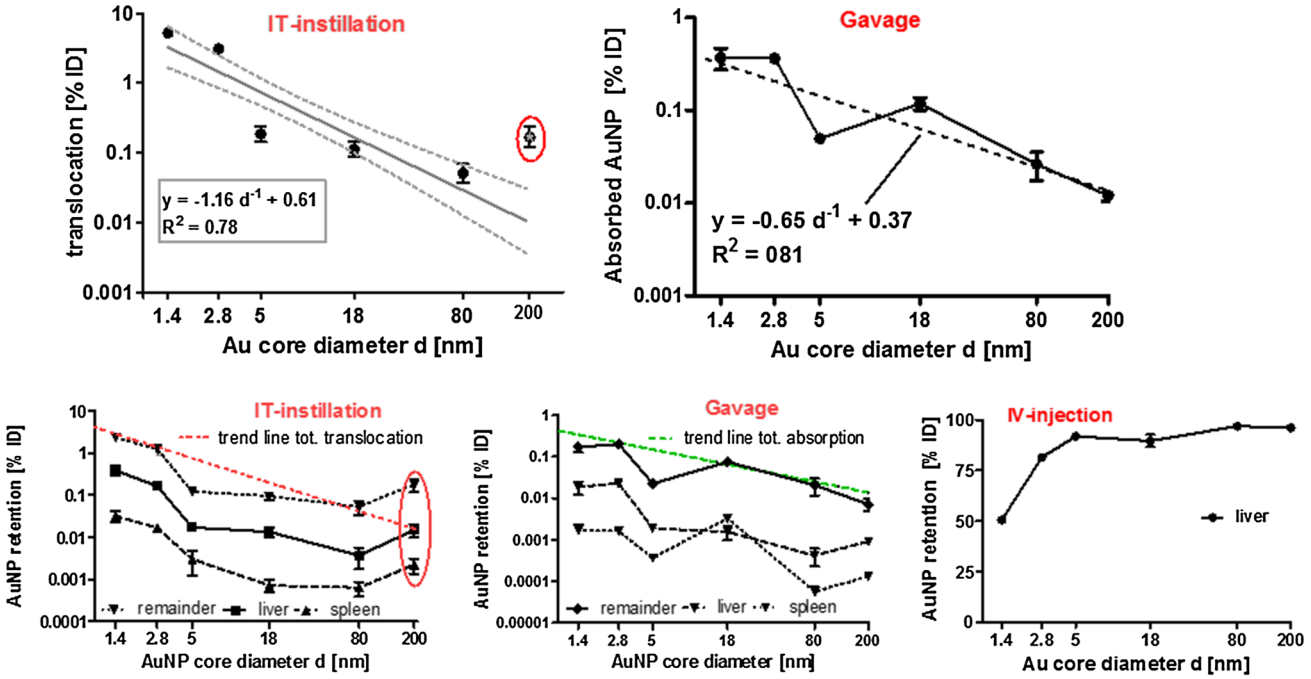

Fig. 25 24 h translocation across the ABB (*upper left panel*) or absorption across the gut epithelium (*upper right panel*) respectively, given as percentage of initially applied dose (ID) of a suite on monodisperse AuNP ranging from 1.4 to 200 nm after either IT-instillation or after gavage (Kreyling et al. 2014; Hirn et al. 2011). A regression line and corresponding equation estimated for 1.4–80 nm AuNP are added. The *lower panels* confirm that this inverse size dependency results from liver, spleen and carcass as indicated by their parallel gradient to the trend line taken from their respective *upper panels*. Mean ± SEM data of $n = 4$ rats for each AuNP size. Note that the AuNPs tested are TPPMS stabilized except the 2.8 nm AuNP, which are stabilized with TGA exhibiting a terminal carboxyl group

within the scientific GIT-physiology community that there is a direct entry across the GIT epithelium into blood vessels (Powell et al. 2010) and lymphatic pathways prior to the entry into circulation are considered to be more realistic. The latter would be congruent with the delayed AuNP arrival in blood causing a steep increase in blood and most organs and tissues between 1 and 24 h (Fig. 24).

The role of rapidly binding serum biomolecules and/or proteins to the AuNP surface, particularly, that of opsonin molecules are intensely discussed in the community but no quantitative data on the trapping contribution of individual molecules are yet determined based on in vivo studies (Monopoli et al. 2013; Zarschler et al. 2016; Docter et al. 2015). Furthermore, what is the role of cellular blood constituents like monocytes, leucocytes, thrombocytes, erythrocytes, etc. interacting with the floating AuNP? Why do cells of the mononuclear phagocytic system (MPS) interact at so different rates of interactions in different organs, like liver versus spleen, kidneys, etc.? The lack of knowledge hampers strongly nanomedicinal drug applications in diagnostics and therapy.

The physicochemical NP properties play a pivotal role in the biokinetics fate: In Fig. 25, the AuNP size-dependent total translocation into blood is shown by integration over all accumulated AuNP in secondary organs and tissues after IT-instillation and gavage. After both applications, there is a linear size-dependent decline from the smallest 1.4 nm particle (Au1.4MS) to 80 nm particle (Au80MS). After IT-instillation translocation declines over almost two orders of magnitude and the decline is proportional to the inverse of the AuNP diameter as indicated by the close to unity slope of the regression line in Fig. 25. This parameter represents the specific AuNP surface area [surface area (μm^2) per volume (μm^3)]; in other words, the translocation across the ABB declines with declining specific surface area (SSA). However, this SSA pattern does no longer apply for 200 nm AuNP after IT-instillation since it is significantly above the regression line. Whether this distinction supports the current upper size limit of 100 nm of nanoparticles versus larger sized particles may be an interesting hint but needs certainly more specific analyses. After gavage, AuNP absorption declines 50-fold with increasing AuNP diameter; but in contrast to IT-instillation the slope of the regression line of absorption across the gut epithelium is no longer unity (i.e., SSA proportional) but about half of it ($SSA^{-0.65}$). Here, the 200 nm AuNPs are fitting to the regression of the AuNP size decline. A physiological explanation of these observations is lacking, but it appears plausible that interactions of AuNP with molecular and cellular constituents of blood as well as with MPS cells of

the various organs and tissues are surface-area dependent, i.e., the larger the surface area per NP volume or mass is the more molecular binding reactions between the AuNP surface and the receptor molecules of cell membranes can take place. Since AuNPs in the circulation are likely not "naked" but coated by serum molecules within seconds to minutes, these binding reactions are modulated by the coating molecules rather than the simple gold surface of AuNP. This increases the possible options of reactions tremendously—which complicates disentangling the role of individual molecule types—but the rate and the capacity by the large number of reactions accelerate largely leading to an effective defense line of the organism.

The lower panels of Fig. 25 show that the size-dependent total accumulation is maintained by liver, spleen and the remaining carcass (comprising the skeleton and soft tissues (like muscle, skin, fat, etc.) since after IT-instillation and gavage the size-dependent translocation/absorption runs parallel to the trend lines taken from Fig. 25. Both size dependencies are very different from that after IV-injection (panel C). In this plot showing a linear *y*-axis, it becomes clear that the smaller the AuNP become the lower their retention in liver which is quite the opposite of SSA proportionality suggesting either the limits of the trapping capacity of Kupffer cells for the huge number of 1.4 or 2.8 nm AuNP or a different physiological trapping mechanism.

When normalizing translocation/absorption in liver, spleen and carcass not as a fraction of ID of IT-instillation or gavage but of the amount of AuNP which had actually entered the circulation followed by accumulation, then the AuNP size dependency between 1.4 and 80 nm disappears grossly in liver and spleen (Fig. 26); this indicates that the larger the AuNPs are the less they translocate/absorb across the ABB/GIT epithelium, respectively, as already shown in Fig. 22. The AuNP size independency holds also for the AuNP accumulation after IV-injection on a logarithmic *y*-axis. Note, however, that both liver and spleen fractions after IT-instillation or gavage are tenfold lower than after IV-injection. More than 50% of the AuNPs which had crossed either ABB or the GIT-epithelium accumulate in the remaining carcass also grossly AuNP size independent; while after IV-injection, the AuNP size-dependent accumulation in the carcass decreases almost 100-fold from 1.4 to 80 nm suggesting that the latter application triggers different mechanisms of accumulation and/or retention when compared to IT-instillation or gavage.

Biokinetics fate depends on pre-engineered AuNP-protein-conjugates (albumin versus Apo-E)

To challenge the role of selected proteins tightly bound on the AuNP surface, we crafted conjugates of either 15 nm or 80 nm monodisperse, ^{198}Au-radiolabeled AuNP with either albumin or apo-lipoprotein E (ApoE) prior to intravenous injection into the tail-vein of adult healthy female C57Bl/6 mice and followed the biokinetics from 30 min to 19 and 48 h (Schäffler et al. 2014). Citrate-stabilized AuNP served as particle controls. For tight protein binding, a double-layer methodology was applied using two polyelectrolyte molecules [polystyrene sulfonate (PSS) and poly-allylamine hydrochloride (PAH)] in between the AuNP surface and the protein (Sousa et al. 2010).

In Fig. 27, accumulation of 15 nm core diameter AuNP in liver, spleen, lungs, brain and the remaining carcass is shown during 48 h. The citrate-stabilized AuNP showed the same biokinetics patterns in mice as those of the sulfonated triphenylphosphine-coated 18 nm AuNP in rats (Figs. 22, 23); i.e., liver retention dominated by far retention in all other organs and the carcass. However, for both HSA-conjugated AuNP (Alb-AuNP) and ApoE-conjugated AuNP (ApoE-AuNP) only about 50 or 70%, respectively, were retained in the liver. About 20% of both conjugates were retained in the spleen and another 20% of Alb-AuNP were found in the lungs; i.e., retentions increased at least tenfold compared to the control-AuNP. In the remaining carcass (comprising skeleton,

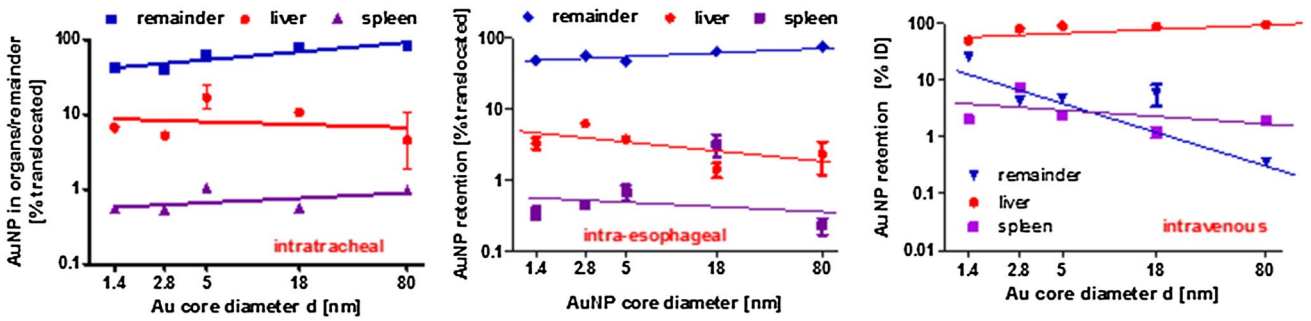

Fig. 26 Size-dependent 24 h retentions in liver, spleen and carcass as percentage of those AuNP which had entered the circulation after crossing the ABB or GIT-epithelium (*panels A + B*) in order to directly compare with the retentions after IV-injection given as percent of ID (*panel C*) (Kreyling et al. 2014; Schleh et al. 2012; Hirn et al. 2011). Data of 200 nm AuNP are not shown. Note that the AuNP tested are TPPMS stabilized except the 2.8 nm AuNP, which are stabilized with TGA exhibiting a terminal carboxyl group

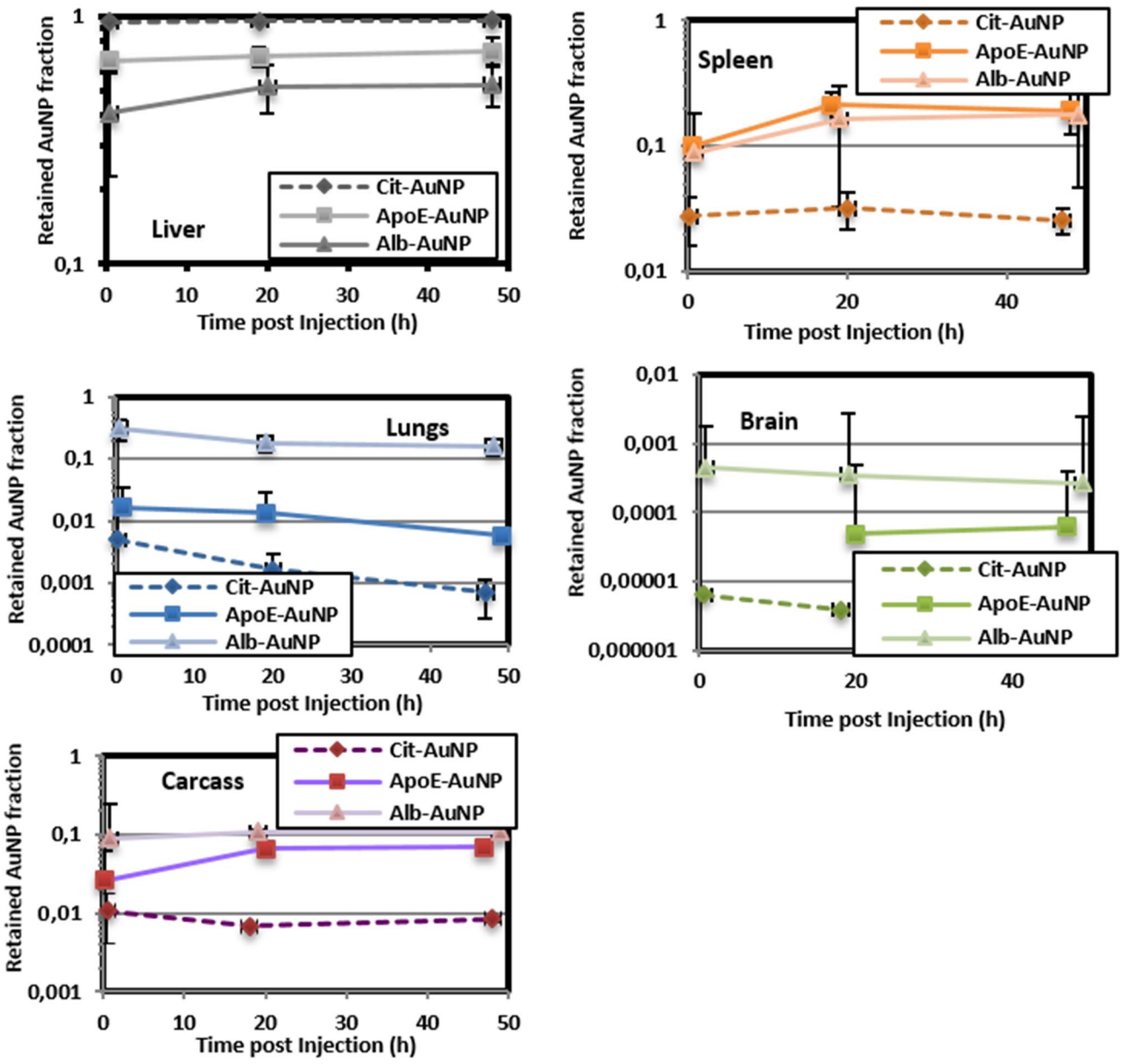

Fig. 27 Retention kinetics and of alb-AuNP, apoE-AuNP, and cit-AuNP (15 nm core diameter) in murine liver, spleen, lungs, brain and carcass are determined at 30 min, 19 h and 48 h after IV-injection (Schäffler et al. 2014). Mean ± SD of AuNP fractions per injected dose; $n = 4$ for each time point

muscles, connective tissue, fat, skin, etc.) Alb-AuNP retention was 10% and that of ApoE-AuNP was 5% which accounted for a tenfold or fivefold increase compared to the control AuNP. Although AuNP conjugate retentions in the brain were below 0.1%, they were 100-fold higher (Alb-AuNP) or tenfold (ApoE-AuNP), respectively, than that of the 15 nm control AuNP. The 80 nm AuNP conjugates showed less pronounced but trend-wise similar differences compared to the 80 nm control AuNP. In summary, these results strongly suggest a pivotal role of tightly bound HSA or ApoE on the biokinetics fate of AuNP. However, we cannot exclude that either of the double-layer fixed proteins stayed on the AuNP surface or may have been exchanged to unknown extends by serum proteins. Therefore, even this rigid study design does not provide a clear-cut answer which fraction of purely coated Alb-AuNP or ApoE-AuNP is retained in which organ or tissue.

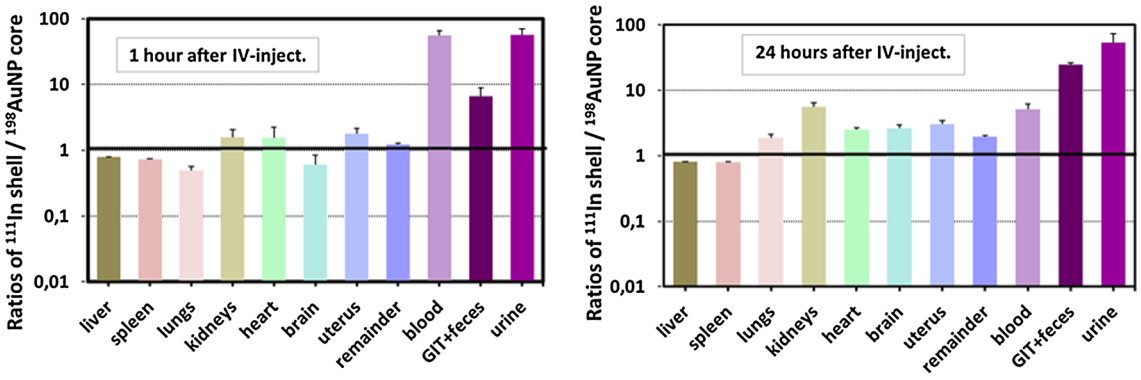

Fig. 28 Ratios of ^{111}In shell to ^{198}AuNP radiolabel in each organ and tissue 1 h and 24 h after IV-injection (Kreyling et al. 2015). AuNP (core diameter 5 nm) with a ^{198}Au core radiolabel grafted with a polymeric, ^{111}In radiolabeled shell were intravenously injected into the tail vein of Wistar–Kyoto rats and their radioactivities were determined in different organs and tissues. The ratios of retentions, given as mean data (±SEM), are denoted as percent of the total radioactivity for the respective radioisotope ($n = 4$ animals per data point). 'Remainder' represents radiolabels found in the rest of the carcass after sampling of organs (e.g., muscles, connective tissue, fat, skin and skeleton). 'GIT + feces' represents the radiolabels found in the gastrointestinal tract and in feces (note that after 1 h no radiolabels were found in feces). 'Blood' represents the total content of radiolabels, as calculated from the measured content in the blood sample and the estimate of the total blood volume. The data show that more ^{111}In shell labels than ^{198}Au core labels were detected in blood, urine, and GIT and feces at any time point. Reprinted by permission from Macmillan Publishers Ltd: Nature Nanotechnology Kreyling et al. (2015) copyright (2015)

In vivo stability of crafted surface modifications on AuNP demonstrated by biokinetics analyses

To show that even firmly grafted polymer shells around AuNP may degrade when injected into rats, synthesized monodisperse, radioactively labeled gold nanoparticles (^{198}Au) and engineered with an ^{111}In-labeled polymer shell around them were IV-injected (Kreyling et al. 2015). Equal biokinetics of both radiolabels would indicate in vivo stability of the nanoparticles, whereas different biodistributions would indicate partial degradation. A shell of the amphiphilic polymer poly(isobutylene-alt-maleic anhydride)-graft-dodecyl was wrapped around the Au core. The chelator 1,4,7,10-tetraazacyclododecane-1,4,7,10-tetraacetic acid (DOTA) was integrated into the polymer shell and was loaded with In (enriched with the radioactive isotope ^{111}In, which acted as the shell label). By calculating the ^{111}In to ^{198}Au ratio for each organ and tissue and each time point, major differences between the retentions of the two radioisotopes became evident (Fig. 28). This differential behavior particularly in blood and excretion indicated dissociation and removal of the ^{111}In label from the shell of the initial AuNP which is more pronounced after 24 h than after 1 h. Further in vitro studies suggest that degradation of the polymer shell is caused by proteolytic enzymes in the liver (Kreyling et al. 2015). These results show that even nanoparticles with high colloidal stability can change their physicochemical properties in vivo.

Size-dependent AuNP crossing of the placenta into fetuses of pregnant rats

Since we have shown above that AuNP can cross various cellular and organ membranes, the question arose whether AuNP can cross the placental membrane entering fetuses during pregnancy. Therefore, we IV injected a subset (1.4, 18, 80 nm) of the suite of different sized AuNP discussed above into the tail vein of pregnant rats in their third trimester (Semmler-Behnke et al. 2014). The biodistribution after 24 h only marginally differed from the non-pregnant control rats; therefore, they correspond grossly to the data given in the Figs. 22, 23, 24, 25 and 26 above. Figure 27 shows that the applied AuNPs accumulate in the uterine wall, the placenta, umbilical cords and the amniotic fluid after IV injection, and eventually they can reach fetuses in a size-dependent manner. However, even with our highly sensitive radio-analytical methodology we were not able to find 80 nm AuNP in the fetuses. A schematic sketch illustrates our observations showing that all three sizes of AuNP can cross the amniotic membrane which is surrounded by the uterine fluid being in exchange with maternal blood; this amniotic membrane crossing occurs by diffusion and/or active cellular transport mechanisms. But only 1.4 and 18 nm AuNP can also cross the placental barrier entering fetal blood circulation and hence the organism of the fetus. Interestingly, the trophoplastic canalicular structure of the placenta prohibits the penetration of 80 nm AuNP into the fetal blood circulation. Furthermore, only the very small 1.4 nm AuNP in the amniotic fluid can cross the fetal skin but not the larger AuNP.

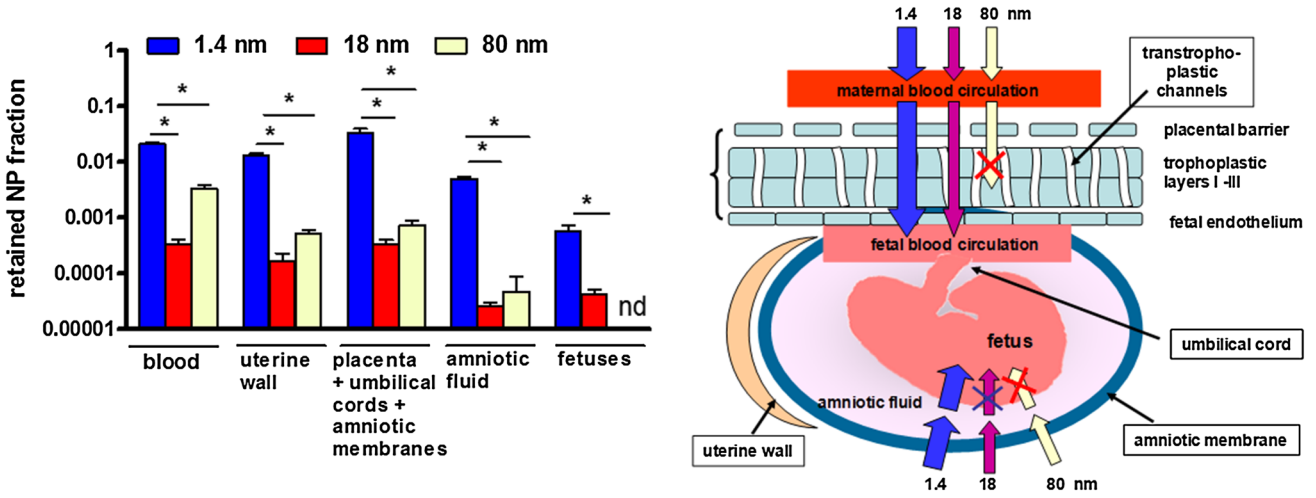

Fig. 29 Retained fractions of IV-injected 1.4, 18 or 80 nm monodisperse AuNP found after 24 h in blood, uterus, placenta and fetuses of pregnant rats (Semmler-Behnke et al. 2014). Data are mean fractions ± SEM, $n = 4$ rats per AuNP size. At the *left side* a sketch illustrating AuNP pathways from the maternal blood towards the fetus. Figure reprinted from Semmler-Behnke et al. (2014)

Disagglomeration-dependent biokinetics of inhaled 40 nm AuNP consisting either of 7 or 20 nm primary AuNP

In many nanomedicinal or nanotechnological AuNP applications not primary AuNP but agglomerates of primary AuNP are likely to be used. When those agglomerates will enter the body the question arises whether these agglomerates stay intact or disagglomerate in the organism (Note any disaggregation of more firmly bound aggregates by chemical bonds is less likely.). This is important since smaller AuNPs distribute differently than larger AuNP as shown above in Figs. 22, 25 and 29. This was demonstrated in comparative inhalation exposures of rats which either inhaled Au-agglomerates of 7 nm primary AuNP or 20 nm primary AuNP (Balasubramanian et al. 2013). Suspensions of either primary AuNP were nebulized yielding airborne Au-agglomerates of about the same size, 46 and 42 nm, respectively, such that the deposition of the inhaled Au-agglomerates was identical in the lungs. As a result, the Au-agglomerates comprising 7 nm primary AuNP [Au-Agg(7 nm)] contained 23-fold more AuNPs than those [Au-Agg(20 nm)] comprising 20 nm AuNP. Inhalation exposures were performed during 15 days (for 6 h/day, 5 days/week for 3 weeks) and the rats were analyzed 2 days after last exposure day by Inductive-Coupled Plasma-Mass Spectroscopy (ICP-MS) analyses of the dissected organs and tissues. After both exposures about 90% Au-mass remained in the lungs and 7.6 versus 8.4%, respectively, were observed in the GIT

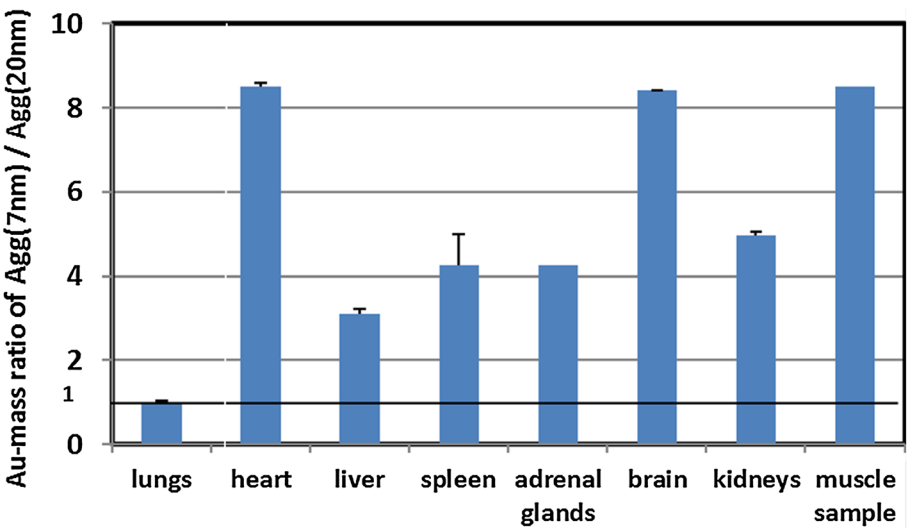

Fig. 30 Ratios of retained Au-masses in lungs, secondary organs and a muscle sample after inhalation exposure to Au-Agg (7 nm) versus Au-Agg (20 nm). Au-masses were determined by ICP-MS. Data are ratios of mean Au-masses of $n = 7$ rats per exposure (Balasubramanian et al. 2013)

and feces as a result of fast mucociliary clearance from the conducting airways; while 2% of the [Au-Agg(7 nm)] versus 0.3% of the [Au-Agg(20 nm)] were translocated across the ABB into blood and accumulated subsequently in secondary organs and tissues. Figure 30 shows that all secondary organs and a muscle sample contain about four times up to eight times more Au-mass after the inhalation of [Au-Agg(7 nm)] when compared to that of [Au-Agg(20 nm)]. In contrast, the ratio of Au-mass in the lungs is about unity. These data demonstrate clearly that the [Au-Agg(7 nm)] disagglomerate to a greater extent and the disagglomerated primary 7 nm AuNP or small clusters of those cross the air-blood barrier of the lungs more readily leading to higher accumulations than primary 20 nm AuNP in all organs and tissues studied. Muscular tissue like heart and the muscle sample accumulate as much as the brain being double that of the other secondary organs studied.

Summary

This review has illustrated that usAuNP can exhibit cytotoxic profile, when the stabilizing ligands allow for direct access to the gold surface either for the direct interaction with biomolecules or for catalytic activity of the unshielded gold surface. Furthermore, it showed that usAuNP exhibits significantly different biodistribution, and enhanced circulation times compared to larger AuNP. In contrast to larger particles, which relatively fast accumulated in the liver, usAuNPs distribute over all other organs as well. The summary of these finding may stimulate the discussion among different disciplines related to (nano)toxicology about possible therapeutic applications of usAuNP that may be anticipated in the future.

References

Alkilany AM, Murphy CJ (2010) Toxicity and cellular uptake of gold nanoparticles: what we have learned so far? J Nanopart Res 12:2313–2333. doi:10.1007/s11051-010-9911-8

Amsterdam A, Nissen RM, Sun Z, Swindell EC, Farrington S, Hopkins N (2004) Identification of 315 genes essential for early zebrafish development. Proc Natl Acad Sci 101(35):12792–12797. doi:10.1073/pnas.0403929101

Balasubramanian SK, Poh KW, Ong CN, Kreyling WG, Ong WY, Yu LE (2013) The effect of primary particle size on biodistribution of inhaled gold nano-agglomerates. Biomaterials 34:5439–5452. doi:10.1016/j.biomaterials.2013.03.080

Bezryadin A, Dekker C, Schmid G (1997) Electrostatic trapping of single conducting nanoparticles between nanoelectrodes. Appl Phys Lett 71(9):1273–1275. doi:10.1063/1.119871

Boda SK, Broda J, Schiefer F, Weber-Heynemann J, Hoss M, Simon U, Basu B, Jahnen-Dechent W (2015) Cytotoxicity of ultrasmall gold nanoparticles on planktonic and biofilm encapsulated Gram-positive Staphylococci. Small 11:3183–3193. doi:10.1002/smll.201403014

Bogart LK, Pourroy G, Murphy CJ, Puntes V, Pellegrino T, Rosenblum D, Peer D, Lévy R (2014) Nanoparticles for imaging, sensing, and therapeutic intervention. ACS Nano 8(4):3107–3122. doi:10.1021/nn500962q

Boyen HG, Kästle G, Weigl F, Koslowski B, Dietrich C, Ziemann P, Spatz JP, Riethmüller S, Hartmann C, Möller M, Schmid G, Garnier MG, Oelhafen P (2002) Oxidation-resistant gold-55 clusters. Science 297(5586):1533–1536. doi:10.1126/science.1076248

Broda J, Schmid G, Simon U (2014) Size- and ligand-specific bioresponse of gold clusters and nanoparticles: challenges and perspectives. In: Mingos DMP (ed) Gold clusters, colloids and nanoparticles I. Springer International Publishing Switzerland, Switzerland, pp 189–241

Broda J, Küster A, Westhues S, Fahrenkamp D, Vogg ATJ, Steitz J, Mottaghy FM, Müller-Newen G, Simon U (2016a) Assessing the intracellular integrity of phosphine-stabilized ultrasmall cytotoxic gold nanoparticles enabled by fluorescence labeling. Adv Healthc Mater 5:3118–3128. doi:10.1002/adhm.201600892

Broda J, Setzler J, Leifert A, Steitz J, Benz R, Simon U, Wenzel W (2016b) Ligand-lipid and ligand-core affinity control the interaction of gold nanoparticles with artificial lipid bilayers and cell membranes. Nanomedicine 12(5):1409–1419. doi:10.1016/j.nano.2015.12.384

Chi L, Hartig M, Drechsler T, Schwaack T, Seidel C, Fuchs H, Schmid G (1998) Single-electron tunneling in Au55 cluster monolayers. Appl Phys A 66(Suppl 1):S187–S190. doi:10.1007/s003390051127

Chowdhury MH, Aslan K, Malyn SN, lakowicz JR, Geddes CD (2006) Metal-enhanced chemiluminescence: radiating plasmons generated from chemically induced electronic excited states. Appl Phys Lett 88:173104. doi:10.1063/1.2195776

Cluskey PD, Newport RJ, Benfield RE, Gurman SJ, Schmid G (1993) An EXAFS study of some gold and palladium cluster compounds. Z Phys D At Mol Clust 26(Suppl 1):8. doi:10.1007/BF01425601

Corain B, Schmid G, Toshima N (2008) Metal nanoclusters in catalysis and materials science: the issue of size control. Elsevier Science, Amsterdam

Crooks RM, Zhao M, Sun L, Chechik V, Yeung LK (2001) Dendrimer-encapsulated metal nanoparticles: synthesis, characterization, and applications to catalysis. Acc Chem Res 34(3):181–190. doi:10.1021/ar000110a

Daniel MC, Astruc D (2004) Gold nanoparticles: assembly, supramolecular chemistry, quantum-size-related properties, and applications toward biology, catalysis, and nanotechnology. Chem Rev 104:293–346. doi:10.1021/cr030698+

Demann ET, Stein PS, Haubenreich JE (2005) Gold as an implant in medicine and dentistry. J Long Term Eff Med Implants 15(6):687–698. doi:10.1615/JLongTermEffMedImplants.v15.i6.100

Docter D, Westmeier D, Markiewicz M, Stolte S, Knauer SK, Stauber RH (2015) The nanoparticle biomolecule corona: lessons learned—challenge accepted? Chem Soc Rev 44:6094–6121. doi:10.1039/c5cs00217f

Dreaden EC, Alkilany AM, Huang X, Murphy CJ, El-Sayed MA (2012) The golden age: gold nanoparticles for biomedicine. Chem Soc Rev 41:2740–2779. doi:10.1039/C1CS15237H

EFSA Panel on Food Additives and Nutrient Sources added to Food (2016) Scientific Opinion on the re-evaluation of gold (E175) as a food additive. EFSA J 14(1):4362. doi:10.2903/j.efsa.2016.436

El-Sayed MA (2003) Optical properties and ultrafast dynamics of metallic nanocrystals. Annu Rev Phys Chem 54:331–366. doi:10.1146/annurev.physchem.54.011002.103759

Esumi K, Tano T, Meguro K (1989) Preparation of organo palladium particles from thermal decomposition of its organic complex in organic solvents. Langmuir 5(1):268–270. doi:10.1021/la00085a051

Esumi K, Tano T, Torigoe K, Meguro K (1990) Preparation and characterization of bimetallic palladium–copper colloids by thermal decomposition of their acetate compounds in organic solvents. Chem Mater 2:564–567. doi:10.1021/cm00011a019

Esumi K, Zuzuki M, Tano T, Torigoe K, Meguro K (1991) Dispersion of uniformly sized palladium particles in organic solvents. Colloids Surf 55:9–14. doi:10.1016/0166-6622(91)80078-3

Esumi K, Sadakane O, Torigoe K, Meguro K (1992a) Preparation of platinum particles by thermal decomposition of platinum complex in organic solvent. Colloids Surf 62(3):255–257. doi:10.1016/0166-6622(92)80008-P

Esumi K, Sato N, Torigoe K, Meguro K (1992b) Size control of gold particles using surfactants. J Colloid Interface Sci 149(1):295–298. doi:10.1016/0021-9797(92)90417-K

FDA (2005) ICH S7B Guideline of FDA (Food and Drug Administration, Rockville, MD). https://www.fda.gov/downloads/Drugs/GuidanceComplianceRegulatoryInformation/Guidances/ucm074963.pdf. Accessed 02 Sept 2013

Fu X, Wang Y, Wu N, Gui L (2002) Shape-selective preparation and properties of oxalate-stabilized pt colloid. Langmuir 18(12):4619–4624. doi:10.1021/la020087x

Geiser M, Kreyling WG (2010) Deposition and biokinetics of inhaled nanoparticles. Part Fibre Toxicol 7:2. doi:10.1186/1743-8977-7-2

Grzelczak M, Pérez-Juste J, Mulvaney P, Liz-Marzán LM (2008) Shape control in gold nanparticle synthesis. Chem Soc Rev 37:1783–1791. doi:10.1039/b711490g

Gutrath BS, Merkens C, Schiefer F, Englert U, Schmid G, Simon U (2013) Isolation, optical properties and core structure of a water-soluble, phosphine-stabilized $[Au_9]^{3+}$ cluster. Z Naturforsch 68b:569–574. doi:10.5560/ZNB.2013-3075

Häkkinen H (2008) Atomic and electronic structure of gold clusters: understanding flakes, cages and superatoms from simple concepts. Chem Soc Rev 37:1847–1859. doi:10.1039/b717686b

Hammer B, Norskov JK (1995) Why gold is the noblest of all the metals? Nature 376(6537):238–240. doi:10.1038/376238a0

He W, Kivork C, Machinani S, Morphew MK, Gail AM, Tesar DB, Tiangco NE, McIntosh JR, Bjorkman PJ (2007) A freeze substitution fixation-based gold enlarging technique for EM studies of endocytosed nanogold-labeled molecules. J Struct Biol 160(1):103–113. doi:10.1016/j.jsb.2007.07.004

Henglein A (2000) Preparation and optical aborption spectra of AucorePtshell and PtcoreAushell colloidal nanoparticles in aqueous solution. J Phys Chem B 104:2201–2203. doi:10.1021/jp994300i

Hirn S, Semmler-Behnke M, Schleh C, Wenk A, Lipka J, Schaffler M, Takenaka S, Moller W, Schmid G, Simon U, Kreyling WG (2011) Particle size-dependent and surface charge-dependent biodistribution of gold nanoparticles after intravenous administration. Eur J Pharm Biopharm 77:407–416. doi:10.1016/j.ejpb.2010.12.029

Homberger M, Simon U (2010) On the application potential of gold nanoparticles in nanoelectronics and biomedicine. Philos Trans R Soc A 368:1405–1453. doi:10.1098/rsta.2009.0275

Jia Y-P, Ma B-Y, Wie X-W, Qian Z-Y (2017) The in vitro and in vivo toxicity of gold nanoparticles. Chin Chem Lett. doi:10.1016/j.cclet.2017.01.021

Ke X, Wang D, Chen C, Yang A, Han Y, Ren L, Li D, Wang H (2014) Co-enhancement of fluorescence and singlet oxygen generation by silica-coated gold nanorods core-shell nanoparticle. Nanoscale Res Lett 9:666. doi:10.1186/1556-276X-9-666

Khlebtsov N, Dykman L (2011) Biodistribution and toxicity of engineered gold nanoparticles: a review of in vitro and in vivo studies. Chem Soc Rev 40:1647–1671. doi:10.1039/C0CS00018C

Kosmehl T, Otte JC, Yang L, Legradi J, Bluhm K, Zinsmeister C, Keiter SH, Reifferscheid G, Manze W, Braunbeck T, Strähle U, Hollert H (2012) A combined DNA-microarray and mechanism-specific toxicity approach with zebrafish embryos to investigate the pollution of river sediments. Reprod Toxicol 33:245–253. doi:10.1016/j.reprotox.2012.01.005

Kreyling WG, Semmler-Behnke M, Takenaka S, Moller W (2013) Differences in the biokinetics of inhaled nano-versus micrometer-sized particles. Acc Chem Res 46:714–722. doi:10.1021/ar300043r

Kreyling WG, Hirn S, Möller W, Schleh C, Wenk A, Celik G, Lipka J, Schäffler M, Haberl N, Johnston BD, Sperling R, Schmid G, Simon U, Parak WJ, Semmler-Behnke M (2014) Air-blood barrier translocation of tracheally instilled gold nanoparticles inversely depends on particle size. ACS Nano 8:222–223. doi:10.1021/nn403256v

Kreyling WG, Abdelmonem AM, Ali Z, Alves F, Geiser M, Haberl N, Hartmann R, Hirn S, de Aberasturi DJ, Kantner K, Khadem-Saba G, Montenegro JM, Rejman J, Rojo T, de Larramendi IR, Ufartes R, Wenk A, Parak WJ (2015) In vivo integrity of polymer-coated gold nanoparticles. Nat Nanotechnol 10:619–623. doi:10.1038/nnano.2015.111

Leifert A, Pan Y, Kinkeldey A, Schiefer F, Setzler J, Scheel O, Lichtenbeld H, Schmid G, Wenzel W, Jahnen-Dechent W, Simon U (2013a) Differential hERG ion channel activity of ultrasmall gold nanoparticles. Proc Natl Acad Sci 110(20):8004–8009. doi:10.1073/pnas.1220143110

Leifert A, Pan-Bartne Y, Simon U, Jahnen-Dechent W (2013b) Molecularly stabilised ultrasmall gold nanoparticles: synthesis, characterization and bioactivity. Nanoscale 5:6224–6242. doi:10.1039/C3NR00916E

Lewinski N, Colvin V, Drezek R (2008) Cytotoxicity of nanoparticles. Small 4(1):26–49. doi:10.1002/smll.200700595

Li W, Chen X (2015) Gold nanoparticles for photoacoustic imaging. Nanomedicine 10(2):299–320. doi:10.2217/nnm.14.169

Li Y, Petroski J, El-Sayed MA (2000) Activation energy of the reaction between hexacyanoferrate(III) and thiosulfate ions catalyzed by platinum nanoparticles. J Phys Chem B 104:1095. doi:10.1021/jp002569s

Liu Y, Meyer-Zaika W, Franzka S, Schmid G, Tsoli M, Kuhn H (2003) Gold-cluster degradation by the transition of B-DNA into A-DNA and the formation of nanowires. Angew Chem Int Ed 42:2853. doi:10.1002/anie.200250235

Marquis BJ, Love SA, Braun KL, Haynes CL (2009) Analytical methods to assess nanoparticle toxicity. Analyst 134:425–439. doi:10.1039/b818082b

Mie G (1908) Beiträge zur Optik trüber Medien, speziell kolloidaler Metallösungen. Ann Phys 330:377–445. doi:10.1002/andp.19083300302

Miller MR, Raftis JB, Langrish JP, McLean SG, Samutrtai P, Connell SP, Wilson S, Vesey AT, Fokkens PHB, Boere AJF, Krystek P, Campbell CJ, Hadoke PWF, Donaldson K, Cassee FR, Newby DE, Duffin R, Mills NL (2017) Inhaled nanoparticles accumulate at sites of vascular disease. ACS Nano. doi:10.1021/acsnano.6b08551 **(Article ASAP)**

Monopoli MP, Pitek AS, Lynch I, Dawson KA (2013) Formation and characterization of the nanoparticle-protein corona. Methods Mol Biol 1025:137–155. doi:10.1007/978-1-62703-462-3_11

Narayanan R, El-Sayed MA (2004) Effect of nanocatalysis in colloidal solution on the tetrahedral and cubic nanoparticle shape: electron-transfer reaction catalyzed by platinum nanoparticles. J Phys Chem B 108(18):5726–5733. doi:10.1021/jp0493780

Ohde H, Wai CM, Kim H, Kim J, Ohde M (2002) Hydrogenation of olefins in supercritical CO_2 catalyzed by palladium nanoparticles in a water-in-CO_2 microemulsion. J Am Chem Soc 124(17):4540–4541. doi:10.1021/ja012232j

Pan Y, Neuss S, Leifert A, Fischler M, Wen F, Simon U, Schmid G, Brandau W, Jahnen-Dechent W (2007) Size-dependent cytotoxicity of gold nanoparticles. Small 3(11):1941–1949. doi:10.1002/smll.200700378

Pan Y, Leifert A, Ruau D, Neuss S, Bornemann J, Schmid G, Brandau W, Simon U, Jahnen-Dechent W (2009) Gold nanoparticles of diameter 1.4 nm trigger necrosis by oxidative stress and mitochondrial damage. Small 5(18):2067–2076. doi:10.1002/smll.200900466

Pan Y, Leifert A, Graf M, Schiefer F, Thoröe-Boveleth S, Broda J, Halloran MC, Hollert H, Laaf D, Simon U, Jahnen-Dechent W (2013) High-sensitivity real-time analysis of nanoparticle toxicity in green fluorescent protein-expressing Zebrafish. Small 9:863–869. doi:10.1002/smll.201201173

Powell JJ, Faria N, Thomas-Mckay E, Pele LC (2010) Origin and fate of dietary nanoparticles and microparticles in the gastrointestinal tract. J Autoimmun 34:J226–J233. doi:10.1016/j.jaut.2009.11.006

Reimers JR, Ford MJ, Marcuccio SM, Ulstrup J, Hush NS (2017) Competition of van der Waals and chemical forces on gold–sulfur surfaces and nanoparticles. Nat Rev Chem 1:0017. doi:10.1038/s41570-017-0017

Rivera-Gil P, De Aberasturi DJ, Wulf V, Pelaz B, Del Pino P, Zhao Y, De La Fuente JM, De Larramend IR, Rojo T, Liang X-J, Parak WJ (2013) The challenge to relate the physicochemical properties of colloidal nanoparticles to their cytotoxicity. Acc Chem Res 46(3):743749. doi:10.1021/ar300039j

Rizzo LY, Golombek SK, Mertens ME, Pan Y, Laaf D, Broda J, Jayapaul J, Möckel D, Subr V, Hennink WE, Storm G, Simon U, Jahnen-Dechent W, Kiessling F, Lammers T (2013) In vivo nanotoxicity testing using the zebrafish embryo assay. J Mater Chem B Mater Biol Med 10(1):3918–3925. doi:10.1039/C3TB20528B

Rosi NL, Giljohann DA, Thaxton CS, Lytton-Jean AK, Han MS, Mirkin CA (2006) Oligonucleotide-modified gold nanoparticles for intracellular gene regulation. Science 312(5776):1027–1030. doi:10.1126/science.1125559

Schaeublin NM, Braydich-Stolle LK, Schrand AM, Miller JM, Hutchison J, Schlager JJ, Hussain SM (2011) Surface charge of gold nanoparticles mediates mechanism of toxicity. Nanoscale 3(2):410–420. doi:10.1039/c0nr00478b

Schäffler M, Sousa F, Wenk A, Sitia L, Hirn S, Schleh C, Haberl N, Violatto M, Canovi M, Andreozzi P, Salmona M, Bigini P, Kreyling WG, Krol S (2014) Blood protein coating of gold nanoparticles as potential tool for organ targeting. Biomaterials 35(10):3455–3466. doi:10.1016/j.biomaterials.2013.12.100

Schleh C, Semmler-Behnke M, Lipka J, Wenk A, Hirn S, Schaffler M, Schmid G, Simon U, Kreyling WG (2012) Size and surface charge of gold nanoparticles determine absorption across intestinal barriers and accumulation in secondary target organs after oral administration. Nanotoxicology 6(1):36–46. doi:10.3109/17435390.2011.552811

Schmid G (1992) Large clusters and colloids. Metals in the embryonic state. Chem Rev 92:1709–1727. doi:10.1021/cr00016a002

Schmid G (1994) Clusters and colloids. Wiley-VCH, Weinheim

Schmid G (2004) Nanoparticles. Wiley-VCH, Weinheim

Schmid G (2008) The relevance of shape and size of Au_{55} clusters. Chem Soc Rev 37:1909–1930. doi:10.1039/B713631P

Schmid G, Bäumle M, Beyer N (2000) Ordered two-dimensional monolayers of Au_{55} clusters. Angew Chem Int Ed Engl 39(1):181–183

Schmid G, Corain B (2003) Nanoparticulated gold: syntheses, structures, electronics, and reactivities. Eur J Inorg Chem 2003:3081–3098. doi:10.1002/ejic.200300187

Schmid G, Simon U (2005) Gold nanoparticles: assembly and electrical properties in 1–3 dimensions. Chem Commun 6:697–710. doi:10.1039/B411696H

Schmid G, Pfeil R, Boese R, Bandermann F, Meyer S, Calis Gijs HM, van der Velden JWA (1981) $Au_{55}[P(C_6H_5)_3]_{12}CI_6$—ein Goldcluster ungewöhnlicher Größe. Chem Ber 114:3634–3642. doi:10.1002/cber.19811141116

Scholz S, Fischer S, Gündel U, Küster E, Luckenbach T, Voelker D (2008) The zebrafish embryo model in environmental risk assessment—applications beyond acute toxicity testing. Environ Sci Pollut Res Int 15(5):394–404. doi:10.1007/s11356-008-0018-z

Semmler-Behnke M, Kreyling WG, Lipka J, Fertsch S, Wenk A, Takenaka S, Schmid G, Brandau W (2008) Biodistribution of 1.4- and 18-nm gold particles in rats. Small 4:2108–2111. doi:10.1002/smll.200800922

Semmler-Behnke M, Lipka J, Wenk A, Hirn S, Schaffler M, Tian F, Schmid G, Oberdorster G, Kreyling W (2014) Size dependent translocation and fetal accumulation of gold nanoparticles from maternal blood in the rat. Part Fibre Toxicol 11:33. doi:10.1186/s12989-014-0033-9

Shaw CF III (1999) Gold-based therapeutic agents. Chem Rev 99(9):2589–2600. doi:10.1021/cr980431o

Smith BA, Zhang JZ, Giebel U, Schmid G (1997) Direct probe of size-dependent electronic relaxation in single-sized Au and nearly monodisperse Pt colloidal nano-particles. Chem Phys Lett 270(1–2):139. doi:10.1016/S0009-2614(97)00339-4

Soenen SJ, Manshian B, Montenegro JM, Amin F, Meermann B, Thiron T, Cornelissen M, Vanhaecke F, Doak S, Parak WJ, De Smedt S, Braeckmans K (2012) Cytotoxic effects of gold nanoparticles: a multiparametric study. ACS Nano 6(7):5767–5783. doi:10.1021/nn301714n

Sousa F, Mandal S, Garrovo C, Astolfo A, Bonifacio A, Latawiec D, Menk RH, Arfelli F, Huewel S, Legname G, Galla HJ, Krol S (2010) Functionalized gold nanoparticles: a detailed in vivo multimodal microscopic brain distribution study. Nanoscale 2(12):2826–2834. doi:10.1039/c0nr00345j

Sousa AA, Morgan JT, Brown PH, Adams A, Jayasekara MPS, Zhang G, Ackerson CJ, Kruhlak MJ, Leapman RD (2012) Synthesis, characterization, and direct intracellular imaging of ultrasmall and uniform glutathione-coated gold nanoparticles. Small 8:2277–2286. doi:10.1002/smll.201200071

Stone V, Miller MR, Clift MJ, Elder A, Mills NL, Møller P, Schins RP, Vogel U, Kreyling WG, Jensen KA, Kuhlbusch TA, Schwarze PE, Hoet P, Pietroiusti A, De Vizcaya-Ruiz A, Baeza-Squiban A, Tran CL, Cassee FR (2016) Nanomaterials vs ambient ultrafine particles: an opportunity to exchange toxicology knowledge. Environ Health Perspect. doi:10.1289/EHP424

Tano T, Esumi K, Meguro K (1989) Preparation of organopalladium sols by thermal decomposition of palladium acetate. J Colloid Interface Sci 133:530–533. doi:10.1016/S0021-9797(89)80069-4

Tsoli M, Kuhn H, Brandau W, Esche H, Schmid G (2005) Cellular uptake and toxicity of Au_{55} clusters. Small. doi:10.1002/smll.200500104

Turner M, Golovko VB, Vaughan OP, Abdulkin P, Berenguer-Murcia A, Tikhov MS, Johnson BF, Lambert RM (2008) Selective oxidation with dioxygen by gold nanoparticle catalysts derived from 55-atom clusters. Nature 454:981–983. doi:10.1038/nature07194

Tyo EC, Vajda S (2015) Catalysis by clusters with precise numbers of atoms. Nat Nanotechnol 10:577–588. doi:10.1038/nnano.2015.140

Verma A, Stellacci F (2010) Effect of surface properties on nanoparticle–cell interactions. Small 6:12–21. doi:10.1002/smll.200901158

Yavuz MS, Cheng Y, Chen J, Cobley CM, Zhang Q, Rycenga M, Xie J, Kim C, Song KH, Schwartz AG, Wang LV, Xia Y (2009) Gold nanocages covered by smart polymers for controlled release with near-infrared light. Nat Mater 8:935–939. doi:10.1038/nmat2564

Zarschler K, Rocks L, Licciardello N, Boselli L, Polo E, Garcia KP, De Cola L, Stephan H, Dawson KA (2016) Ultrasmall inorganic nanoparticles: state-of-the-art and perspectives for biomedical applications. Nanomedicine 12:1663–1701. doi:10.1016/j.nano.2016.02.019

Zhang H, Schmid G, Hartmann U (2003) Reduced metallic properties of ligand-stabilized small metal clusters. Nano Lett 33(3):305–307. doi:10.1021/nl0258980